

Analyzing power measurements for $^{209}\text{Bi}(n,n)$ at 6 and 9 MeV and consistent dispersive optical-model analyses for $n+^{209}\text{Bi}$ and $n+^{208}\text{Pb}$ from -20 to $+80$ MeV

G. J. Weisel,* W. Tornow, C. R. Howell, P. D. Felsher,† M. AlOhalil, M. L. Roberts,‡ R. K. Das, and R. L. Walter
Department of Physics, Duke University and Triangle Universities Nuclear Laboratory, Durham, North Carolina 27708-0308

G. Mertens

Physikalisches Institut, University of Tübingen, Federal Republic of Germany

(Received 13 May 1996)

High-accuracy measurements of $A_y(\theta)$ data for elastic scattering for $n+^{209}\text{Bi}$ have been performed at 6 and 9 MeV. The data are incorporated into a large database of $\sigma(\theta)$, $A_y(\theta)$, and σ_T for $n+^{209}\text{Bi}$ covering the energy range 1.0–80 MeV. A complementary database is constructed for $n+^{208}\text{Pb}$ and a dispersive optical-model analysis is performed for both scattering systems while constraining many of the parameters to be identical for both systems. A good representation of both databases is obtained with conventional geometry and spin-orbit parameters. The ^{208}Pb model predicts quite well the measured energies of valence single-particle and single-hole bound states. Occupation probabilities and spectroscopic factors for the same bound states are also calculated. Finally, a fully constrained model is presented in which the only differences between the $n+^{208}\text{Pb}$ and the $n+^{209}\text{Bi}$ systems are the Fermi energy and the isospin dependence in the real volume potential. [S0556-2813(96)00611-5]

PACS number(s): 24.10.Ht, 25.40.Dn, 24.70.+s, 28.20.Cz

I. INTRODUCTION

In the past eight years there has been a concerted effort to apply the dispersion relation of the optical model to nucleon-nucleus scattering to determine the nuclear mean field in finite nuclear matter. The dispersive optical model (DOM) for nucleon-nucleus scattering has had its main impact in two ways: (i) the DOM allows for a physically self-consistent way to introduce energy dependencies into the real part V and imaginary part W of the nuclear potential given by $U(r,E) = V(r,E) + iW(r,E)$ and (ii) the DOM provides a natural extension of an optical model derived from scattering data into the negative energy regime, i.e., into the bound-state or shell-model region. In this way, the DOM gives a consistent and continuous description of the nucleon-nucleus interaction from negative to positive energies. Mahaux and co-workers [1] were the first to demonstrate that the nuclear structure properties, such as single-particle occupation probabilities, strength functions, and energies derived from the DOM for nucleon-nucleus scattering, are consistent to a large extent with properties determined from nucleon transfer and inelastic electron scattering measurements, in particular for the system $n+^{208}\text{Pb}$.

At the Triangle Universities Laboratory (TUNL) we have been interested in measuring analyzing power $A_y(\theta)$ data to constrain the characterization of the nucleon-nucleus interaction in general and to parametrize the spin-orbit interaction

in particular. In Roberts *et al.* [2] we reported high-accuracy $A_y(\theta)$ data from 6 to 10 MeV and $\sigma(\theta)$ data at 9 MeV for $^{208}\text{Pb}(n,n)$. In Ref. [2] we presented a DOM analysis of $^{208}\text{Pb}(n,n)$ differential scattering data from 5 to 40 MeV, and $n+^{208}\text{Pb}$ total cross section σ_T data from 2 to 80 MeV. Although the DOM of Ref. [2] gave a good description of the data, there were a number of deficiencies in the formulation of the model and its agreement with the data. One weakness in the model was that we assumed that the energy dependence of the volume absorptive potential could be represented by a single linear segment and the surface absorptive potential by two linear segments. Further weaknesses of the model relate to the contributions of Mahaux and Sartor [1] who have pointed out that (i) due to nonlocality effects, the absorptive potential used in the dispersion relation will be highly asymmetric (with respect to the Fermi energy E_F) for $|E| > 60$ MeV and (ii) that there should be a gap centered about E_F in which the absorption term drops to zero, i.e., at least for energies between the first-hole and first-particle states. In the analysis of Roberts *et al.* [2] we assumed that the absorptive potentials were symmetric about E_F and that they were nonzero in the energy gap surrounding E_F . Finally, in Ref. [2] we used a nonrelativistic optical-model code. Since the database extends up to 80 MeV and since the recent σ_T data are very accurate, i.e., the uncertainty $\Delta\sigma_T$ is about $\pm 1\%$, it is now important to consider relativistic corrections.

One of the disappointments of the DOM predictions of Roberts *et al.* [2] was the description of the $\sigma(\theta)$ and $A_y(\theta)$ data in the 4.0 to 7.5 MeV region. One obvious concern is whether the calculated contributions from compound-nucleus (CN) elastic scattering are accurate. Because the measured $\sigma(\theta)$ for $^{209}\text{Bi}(n,n)$ is nearly identical to that for $^{208}\text{Pb}(n,n)$ at energies above 8 MeV, we decided to make a complementary DOM analysis of the $^{209}\text{Bi}(n,n)$ data. Below

*Present address: Department of History, 4131 Turlington Hall, University of Florida, Gainesville, FL 32611-2036.

†Present address: EG&G Rocky Flats, Inc., P.O. Box 464, Bldg. 886, Golden, CO 80402-0464.

‡Present address: Center for Atomic Mass Spectroscopy, Lawrence Livermore National Laboratory, Livermore, CA 94550.

8 MeV, the CN elastic scattering for $^{209}\text{Bi}(n,n)$ is less than that for $^{208}\text{Pb}(n,n)$. Therefore, if there is inaccuracy in the CN calculations, it would be less critical for $^{209}\text{Bi}(n,n)$. In order to provide additional constraints on a model for $^{209}\text{Bi}(n,n)$ we measured the $A_y(\theta)$ at 6 and 9 MeV. The 9 MeV data were obtained to see if it exhibited the identical features as had been observed for ^{208}Pb , since at 9 MeV the CN elastic scattering is calculated to be negligible for both nuclei. The 6 MeV data were obtained to document the differences between $A_y(\theta)$ for ^{208}Pb and ^{209}Bi ; it was known that at this energy the CN elastic scattering was significant for both nuclei.

The organization of the paper is the following. Section II describes the experimental procedures and the corrections for multiple scattering, etc., within the scatterer. Section III discusses the CN calculations. Section IV introduces the $^{208}\text{Pb}(n,n)$ and $^{209}\text{Bi}(n,n)$ databases. Section V provides an outline of the dispersion-relation optical model and the forms of the energy and radial dependencies of the real, imaginary, and spin-orbit potentials. Section VI describes the revised GENOA search code, our procedure for searching, and the resulting DOM potentials for $^{208}\text{Pb}(n,n)$ and $^{209}\text{Bi}(n,n)$. Section VII presents a brief discussion of properties of single-particle bound states for $n+^{208}\text{Pb}$.

This brief introductory section omitted references to other reports on conventional or dispersive optical-model analyses for ^{208}Pb and ^{209}Bi . Many of the early DOM references are given in the review by Mahaux and Sartor [1]; the most pertinent ones will be mentioned below. However, here we would like to mention the seminal analysis by Annand, Finlay, and Dietrich [3] who developed a combined standard optical model for $n+^{209}\text{Bi}$ and $n+^{208}\text{Pb}$. The present paper is based on a Ph.D. dissertation [4].

II. EXPERIMENTAL TECHNIQUE

The $A_y(\theta)$ data for $^{209}\text{Bi}(n,n)^{209}\text{Bi}$ were obtained at the tandem Van de Graaff accelerator facility of the Triangle Universities Nuclear Laboratory (TUNL). Much of the data were accumulated back to back with the complementary measurements for $^{208}\text{Pb}(n,n)$ that were reported by Roberts *et al.* [2]. Considerable detail is given there about our technique for $A_y(\theta)$ measurements and about the corrections applied to obtain final values for $A_y(\theta)$.

A brief outline of the method is given here. Polarized neutrons were scattered from a cylinder of ^{209}Bi (2.0 cm in diameter and 3.3 cm in height) and detected in pairs of scintillators placed symmetrically on opposite sides of the incident neutron beam axis. Two massively shielded detectors were utilized for forward angle measurements and sometimes four additional shielded detectors were utilized at the backward angles. All of the detectors were liquid-organic scintillators that permitted pulse-shape discrimination against γ -ray induced events.

The polarized neutron beam was obtained from the $^2\text{H}(\vec{d},\vec{n})^3\text{He}$ reaction using a polarized deuteron beam that originated in the TUNL Lamb-shift polarized ion source. Neutrons emitted at the 0° reaction angle were incident on the cylindrical ^{209}Bi scatterer, whose axis was oriented normal to the horizontal reaction plane containing the neutron detector array. The deuteron beam polarization was deter-

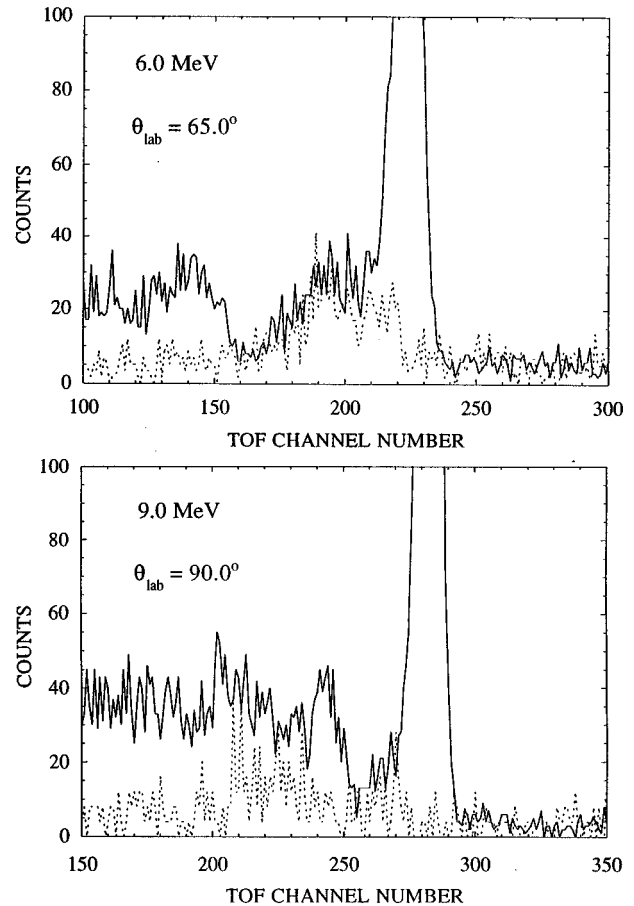


FIG. 1. Typical TOF spectra for 6.0 MeV at $\theta_{\text{lab}}=65^\circ$ and 9.0 MeV at $\theta_{\text{lab}}=90^\circ$: sample-in counts (solid) and sample-out counts (dotted).

mined with the quench-ratio technique [5]. The polarization transfer coefficient for the $^2\text{H}(\vec{d},\vec{n})^3\text{He}$ reaction was taken from the measurements of Lisowski *et al.* [6]. The absolute value of the neutron polarization was known to an accuracy of about $\pm 3\%$. The spread in neutron energy was mainly caused by the deuteron energy loss in the gas of the deuterium cell; the spreads were 350 and 420 keV at 6 and 9 MeV, respectively.

The deuteron beam was bunched and chopped to obtain 2 ns bursts. The scattered neutrons were detected in a time-of-flight mode with an overall system resolution of about 3 ns. Sample spectra are illustrated in Fig. 1 where we also show spectra recorded with the ^{209}Bi sample removed. The time scale is about 0.16 ns per channel. An expanded view of the spectra that result when the sample-removed counts are subtracted from the sample-in spectra is shown in Fig. 2. (Note the zero offset for the ordinate.) The $\frac{7}{2}^-$ label indicates the location for inelastic scattering to the first excited state of ^{209}Bi at 0.897 MeV. There is a small sample-correlated background that is apparent on the right side of the elastic-scattering peak. It was assumed that this background was a “white” background originating from neutrons scattered throughout the target room; a flat background of this level was subtracted from the entire spectrum. The small residual background in the valley between the $\frac{7}{2}^-$ and the elastic-scattering peaks are sample correlated and caused by neu-

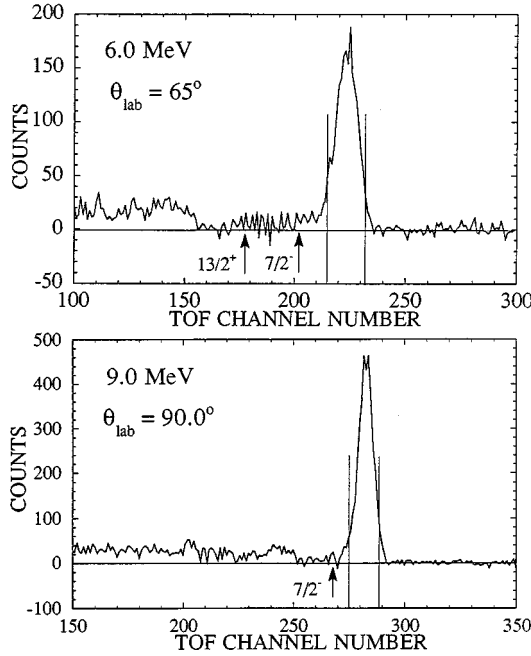


FIG. 2. The difference spectra for the examples of Fig. 1 with backgrounds and summing window displayed.

trons, for example, that scatter first from the shadow bar and then from the ^{209}Bi scatterer. These latter events are unimportant in $A_y(\theta)$ measurements as long as they lie outside of the summing window chosen for the elastic-scattering peak. Examples of the choice of windows that were used in the analysis are indicated by the vertical lines in Fig. 2.

The Monte Carlo code JANE obtained from Woye [7] was used to correct the measured asymmetries for finite-geometry effects, taking into account the sizes of the deuterium gas cell, the scatterer, and the detector, as well as attenuation and multiple scattering of the neutrons in the scatterer. The data presented here are values of $A_y(\theta)$ for the effective angle of the observation as obtained from JANE. Although the statistical uncertainties of the original on-line values were under about $\pm 3\%$, because of sizable multiple-scattering contributions in the valleys of the differential cross section, the final uncertainties for singly scattered events were more than a factor of 2 larger in these angular regions. The final data (solid circles) are shown in Fig. 3 alongside the uncorrected original data (open circles). Some of these data points required more than 6 h to measure. To check for physical consistency, the product $A_y(\theta) \times \sigma(\theta)$ was fit with an associated Legendre polynomial expansion. The $\sigma(\theta)$ values used in this procedure were obtained from Lawson *et al.* [8] at 6 MeV and Das and Finlay [9] at 9 MeV. The solid and dashed curves show the results of this fitting procedure for the uncorrected and final data, respectively. All the final $A_y(\theta)$ data in Fig. 3 are statistically consistent with this fitting approach.

III. COMPOUND-NUCLEUS CORRECTIONS

In OM studies on $n + ^{208}\text{Pb}$ there are difficulties in describing the $\sigma(\theta)$ data in the energy range $4.0 \text{ MeV} \leq E \leq 7.5 \text{ MeV}$. Several unusual approaches like

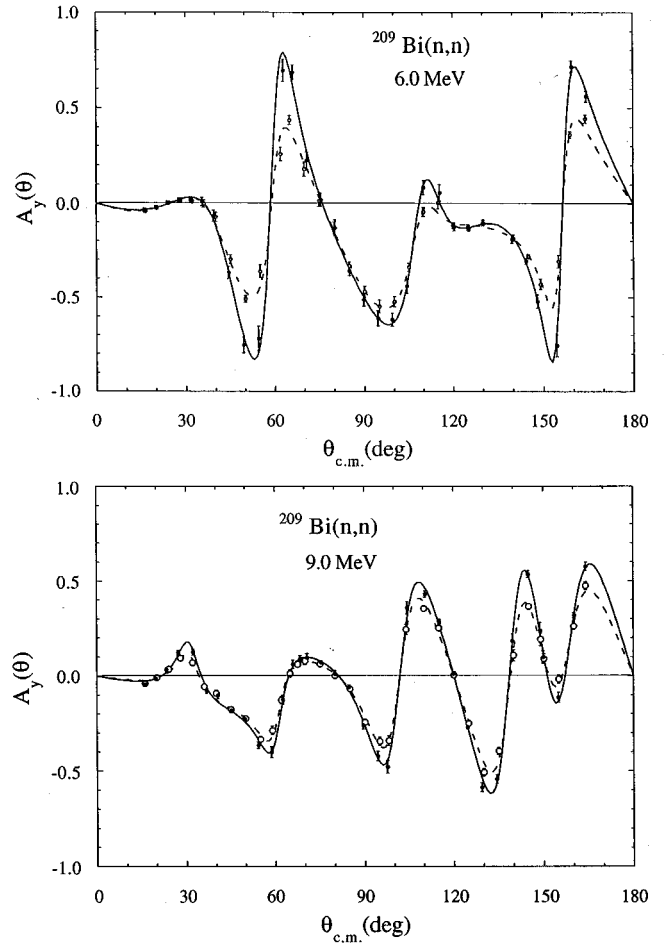


FIG. 3. The $^{209}\text{Bi}(n,n)$ $A_y(\theta)$ at $E_n = 6.0$ and 9.0 MeV before (dotted) and after (solid) finite geometry corrections.

ℓ -dependent absorption and energy dependent geometries have been introduced in attempts to explain this problem. However, in this energy range the compound-nucleus elastic scattering contributes appreciably to $\sigma(\theta)$. Therefore, we felt that it was important to investigate the accuracy of the calculated compound nucleus yield.

We used the statistical model of nuclear reactions to compute the CN contributions to the elastic channel. When the cross section is averaged over many CN resonances, as in the present data set, the shape-elastic (SE) differential cross section may be taken as the experimentally observed (ob) cross section minus the CN elastic-scattering contribution:

$$\sigma^{\text{SE}}(\theta) = \sigma^{\text{ob}}(\theta) - \sigma^{\text{CN}}(\theta). \quad (1)$$

We assume that the analyzing power of the CN contribution is zero through the process of averaging over many CN resonances. Thus, the effect the CN elastic-scattering contribution is to merely dilute the magnitude of $A_y^{\text{SE}}(\theta)$ produced by the contribution from shape-elastic scattering. In this case, the desired $A_y^{\text{SE}}(\theta)$ is related to the observed analyzing power $A_y^{\text{ob}}(\theta)$ as

$$A_y^{\text{SE}}(\theta) = \frac{\sigma^{\text{ob}}(\theta)}{\sigma^{\text{SE}}(\theta)} A_y^{\text{ob}}(\theta). \quad (2)$$

The statistical-model calculations require the following as input: (i) inclusion of all significant reaction channels; (ii) an OMP for each reaction channel; (iii) known discrete excitations of each residual nucleus; (iv) a choice of “width-fluctuation corrections”; (v) a model for a continuum of the excited states extending beyond the known levels. For the present work, the only significant exit channels are (n,n') since the high nuclear charge of ^{208}Pb and ^{209}Bi suppresses all charged-particle channels at the energies where the $\sigma^{\text{CN}}(\theta)$ is significant. Our CN calculations used the $^{208}\text{Pb}(n,n)$ and $^{209}\text{Bi}(n,n)$ OM potentials of Annand *et al.* [3]. Checks of the CN calculations, using the DOM’s of the present study, did not demonstrate any significant differences from the results reported in this section. Discrete excitation levels are available from nuclear data tables: Ref. [10] for ^{208}Pb and Ref. [11] for ^{209}Bi . The approach of Moldauer [12,13] was used to calculate the width-fluctuation correction since this method proved to be the most reliable in the careful study by Annand *et al.* [3].

The CN calculation is highly sensitive to the parameters modeling the continuum of excited states. We used the “constant temperature” (CT) formula [14] to estimate the number of excited states available to the scattering system at excitation energy E ; that is, $N(E) = \exp[(E - E_o)/T]$, where T is the “nuclear temperature” and E_o the “offset energy.” These two parameters are determined by three criteria: (i) extrapolation from a plot of the number of available states vs excitation energy; (ii) consideration of the $A_y(\theta)$ data, which sets an upper limit to the CN correction, since the magnitude of $A_y(\theta)$ cannot exceed 1.0; (iii) reasonable agreement between available inelastic-scattering data and results of the CN calculation. Criterion (i) is the most important consideration. In the case of criterion (iii), not much inelastic data are available at low energies and these data are subject to large error bars.

As a test of our CN calculations, we compared our $^{209}\text{Bi}(n,n)A_y(\theta)$ data at 6.0 and 9.0 MeV to corresponding data for $^{208}\text{Pb}(n,n)$ reported by Roberts *et al.* [2]. From a shape-elastic point of view the $\sigma(\theta)$ and $A_y(\theta)$ data for $^{208}\text{Pb}(n,n)$ and $^{209}\text{Bi}(n,n)$ should only differ a slight amount due to the 0.15% difference in nuclear radii. So, large differences in the observed data might be attributed to the different CN contributions. The CN calculations were accomplished with the computer codes HELGA [15] and OPSTAT [16]. The calculations showed that the compound-elastic contributions were negligible for both $^{208}\text{Pb}(n,n)$ and $^{209}\text{Bi}(n,n)$ at 9.0 MeV. Figure 4 shows the 9.0 MeV ^{209}Bi data and companion ^{208}Pb data. The data and corresponding polynomial fits demonstrate the close similarity of the $\sigma(\theta)$ and $A_y(\theta)$ for these two nuclei.

However, at 6.0 MeV the compound-elastic contributions are significant for both nuclei. For ^{209}Bi , the first 25 discrete levels were used, covering the region up to an excitation energy of 3.23 MeV. Beyond this energy, the CT formula was used to model the continuum. Displayed in the bottom panel of Fig. 5 is the sum of the discrete states for ^{209}Bi , as well as the CT extrapolation used. Table I lists the CT parameters (T and E_o) used for all CN calculations, as well as the resulting integrated compound-elastic cross sections σ_T^{CE} . The calculated $\sigma^{\text{CN}}(\theta)$ for elastic scattering from ^{209}Bi is illustrated in Fig. 6 (top panel) by the solid curve at

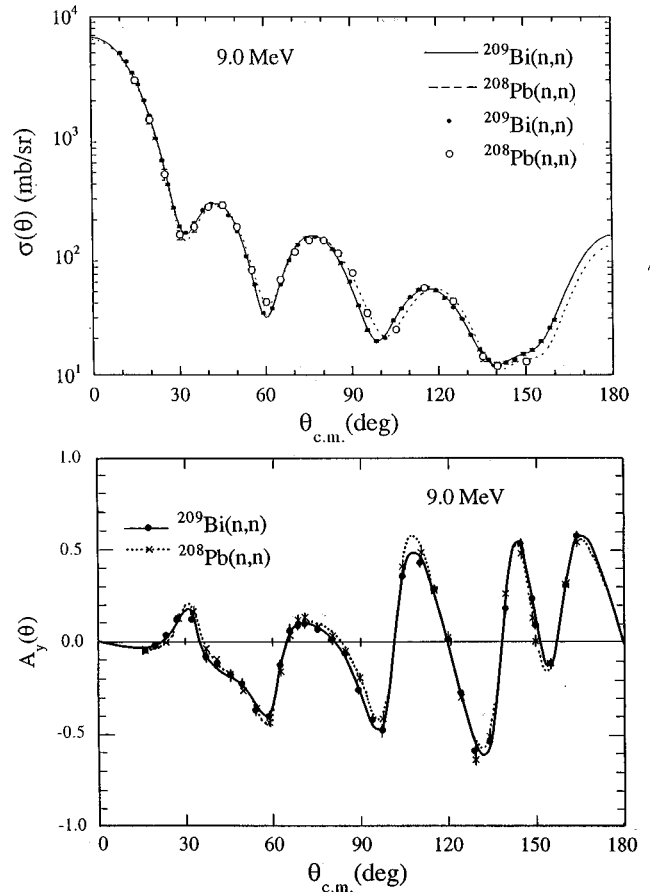


FIG. 4. The $\sigma(\theta)$ and $A_y(\theta)$ at $E_n = 9.0$ MeV for $^{209}\text{Bi}(n,n)$ and $^{208}\text{Pb}(n,n)$. The curves are polynomial fits: ^{209}Bi (solid) and ^{208}Pb (dotted).

the level of about 3 mb/sr. The data points represent the values of $\sigma^{\text{SE}}(\theta)$ that we obtained after subtraction of $\sigma^{\text{CN}}(\theta)$ from the $\sigma^{\text{ob}}(\theta)$ measured by Lawson *et al.* [8]. The solid curve is a Legendre polynomial expansion fit to $\sigma^{\text{SE}}(\theta)$. In the lower panel of Fig. 6 we display values of $A_y^{\text{SE}}(\theta)$ for ^{209}Bi obtained by applying the CN correction according to Eq. (2). Here, the solid curve is again derived from fitting the values for the product $A_y^{\text{SE}}(\theta) \times \sigma^{\text{SE}}(\theta)$ with an associated Legendre polynomial expansion.

Our choice of CT parameters for the ^{209}Bi calculation at 6.0 MeV was severely constrained by the second criterion, since the $A_y(\theta)$ distribution already is close to 1.0 before the application of Eq. (2). In the case of ^{208}Pb , a wider range of CN corrections is allowed by the second criterion, since the observed $A_y(\theta)$ values are not close to 1.0. To examine the range of possible CN corrections for ^{208}Pb , we made two CN calculations with two choices of CT parameters. For both determinations of the CT parameters, we explicitly included the first 25 discrete states for ^{208}Pb , in order to match the calculation for ^{209}Bi . In our first choice, which we denote by “all observed,” we forced the continuum to follow the 126 known ^{208}Pb discrete levels [10] in the energy range 4.32 – 6.0 MeV (see the solid line in the top panel of Fig. 5). In our second choice, we constructed a continuum which assumes that only half of the discrete states up to 6.0 MeV have been observed (labeled “50% unobserved”). This second choice

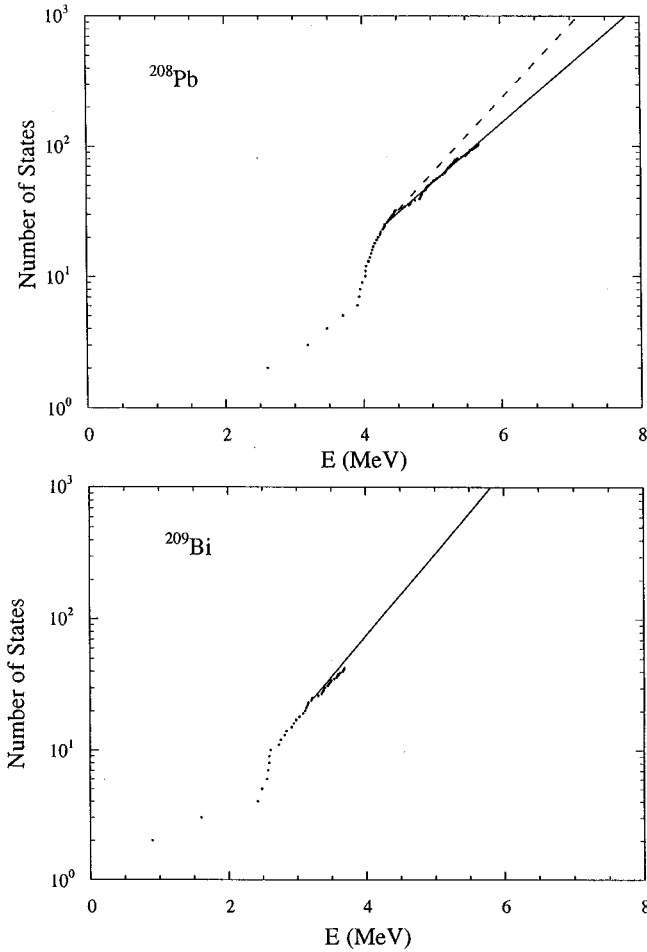


FIG. 5. Display of discrete states and the continuum representation used in the CN calculations at $E_n = 6.0$ MeV for $^{209}\text{Bi}(n,n)$ and $^{208}\text{Pb}(n,n)$. For $^{208}\text{Pb}(n,n)$, two choices of the continuum are shown: the “all observed” case (solid curve) and the “50% unobserved” case (dashed).

of CT parameters, shown by the dashed curve of Fig. 5, is unrealistic, but is intended as a limiting case.

The $\sigma^{\text{CN}}(\theta)$ for ^{208}Pb are shown in Fig. 6 by the dotted curve for the “all observed” case and by the dashed curve for the “50% unobserved” case. These two $\sigma^{\text{CN}}(\theta)$ were subtracted from the $\sigma^{\text{ob}}(\theta)$ data at 6.0 MeV of Annand *et al.* [3]. The resulting $\sigma^{\text{SE}}(\theta)$ were fit by Legendre polynomial expansions, which are shown by the dotted and dashed curves in the top panel of Fig. 6. The $A_y(\theta)$ data for ^{208}Pb of Roberts *et al.* [2] were correspondingly adjusted for CN contributions and fit with polynomial expansions. The results are indicated by the dotted and dashed curves in the lower panel

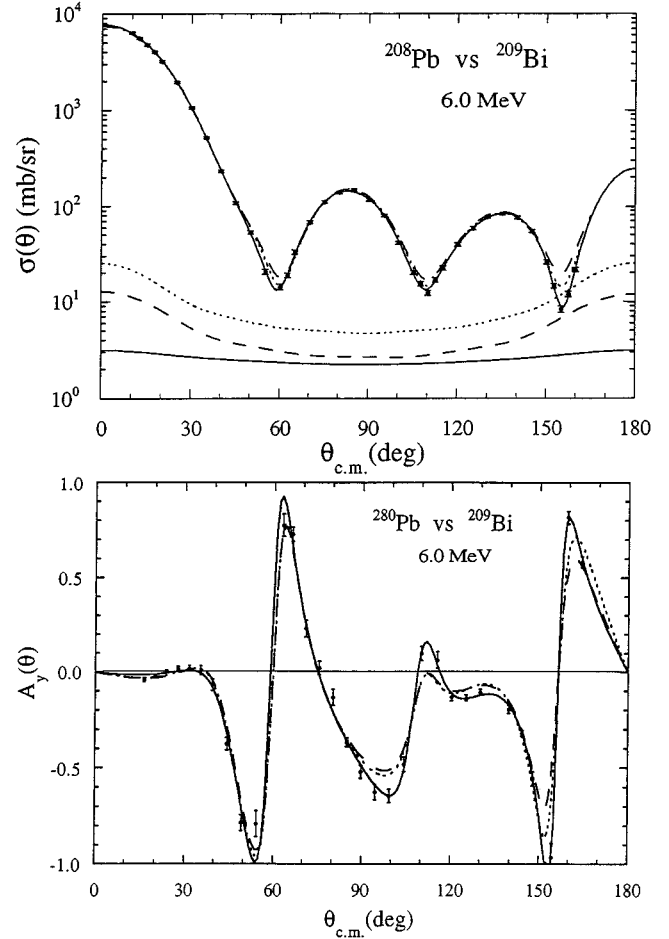


FIG. 6. The CN corrected $\sigma(\theta)$ and $A_y(\theta)$ data at $E_n = 6.0$ MeV: $^{209}\text{Bi}(n,n)$ data and polynomial fit (solid), compared to polynomial fits to $^{208}\text{Pb}(n,n)$ data corrected with the “all observed” CN calculation (dotted) and the “50% unobserved” CN calculation (dashed). The respective CN contributions for each are displayed with the same key.

of Fig. 6. Note that the “all observed” CN-corrected $^{208}\text{Pb}(n,n)$ data are in close agreement with the CN-corrected $^{209}\text{Bi}(n,n)$ data. However, small differences, which are too large to be attributed to radial sizes, remain between these two data sets, particularly in the angular region where $\sigma(\theta)$ is small.

After these preliminary calculations, we performed a final set of CN calculations for ^{208}Pb for our DOM analysis. We used the first 50 discrete states of ^{208}Pb ; that is, we assumed that all levels have been found up to the corresponding excitation energy of $E = 4.95$ MeV. Above this energy, we

TABLE I. Constant temperature parameters and calculated values for the CN integrated elastic scattering cross section at 6.0 MeV.

		T (MeV)	E_o (MeV)	σ_T^{CE} (mb) Present	σ_T^{CE} (mb) Ref. [3]
^{208}Pb w/25 levels	50% unobserved	0.74	1.91	59	—
	All observed	0.95	1.27	81	—
^{208}Pb w/50 levels	Used for DOM	0.87	1.57	78	≈ 49
^{209}Bi w/25 levels	Used for DOM	0.70	0.98	32	≈ 44

chose the parameters of the CT formula to lay between the two extreme limits considered above. The final data for both ^{208}Pb and ^{209}Bi at 6.0 MeV using the ‘‘DOM’’ CT parameters of Table I are displayed in Fig. 6. An uncertainty of $\pm 15\%$ was assigned to all CN calculations and then propagated to the $\sigma^{\text{SE}}(\theta)$ and $A_y^{\text{SE}}(\theta)$. This caused large error bars for the data in the angular regions where $\sigma^{\text{SE}}(\theta)$ is small.

As a check, we compared the final CN calculations for the integrated cross sections with some available (n,n') data from Refs. [3,17] at several incident neutron energies. These comparisons showed good agreement. For example, consider inelastic scattering through the 1.608 MeV, $J^\pi = \frac{13}{2}^+$ excited state of the $n + ^{209}\text{Bi}$ system. The experimental cross sections at $E_n = 4$ and 6 MeV are 195 mb and 20 mb, respectively; our CN calculation yielded 197 mb and 16 mb, respectively. For inelastic scattering through the 3.198 MeV, $J^\pi = 5^-$ excited state of the $n + ^{208}\text{Pb}$ system, the experimental cross section at $E_n = 6$ MeV is 86 mb; our CN calculation yielded 65 mb.

Overall, we prefer our CN corrections to those of Annand *et al.* [3]. Note from Table I that, relative to our CN results, those of Ref. [3] slightly undercorrect the ^{208}Pb data and overcorrect the ^{209}Bi data. At most energies, the CN corrections of Ref. [3] bring about stronger differences between the $\sigma^{\text{SE}}(\theta)$ and $A_y^{\text{SE}}(\theta)$ data sets for ^{208}Pb and ^{209}Bi than exhibited in our CN-corrected data.

However, we report a problem encountered in the CN correction of the ^{209}Bi data for $E_n < 3.5$ MeV. The calculations, using either the OM parameters of Ref. [3] or our present DOM’s, resulted in CN elastic contributions in the 1.46–3.47 MeV range which had values greater than the measured $\sigma(\theta)$ in the region of the deepest minima. This unphysical result cannot be due to the CT parameters since for this low energy region we have explicitly included all the discrete states. It appears that for $^{209}\text{Bi}(n,n)$ the statistical model for CN reactions is not totally valid below 3.5 MeV. One possible approach to resolving the problem would be to alter the only free parameters left to the CN calculation at these low energies: those of the optical model. However, this leads to an abnormal model, one which cannot accurately describe the data over any appreciable energy regime. [It appears that Ref. [3] used such an OM for its CN corrections for $^{209}\text{Bi}(n,n)$ below 3.5 MeV.] Since such a model is not in the spirit of a ‘‘normal’’ optical model, we renormalized the ^{209}Bi 1.46, 1.97, 2.46, 2.97, and 3.47 MeV compound-elastic calculations (which included the Moldauer width-fluctuation corrections) with the multiplicative factors 0.81, 0.81, 0.94, 0.94, and 0.94, respectively. These factors keep the final $\sigma^{\text{SE}}(\theta)$ data positive valued and produced a reasonable energy dependence for the deep minima in $\sigma^{\text{SE}}(\theta)$. While this renormalization strategy is not much more appealing than the ‘‘abnormal OM’’ option, it does allow us to retain our CN calculations at higher energies, which we demonstrated above as being an improvement over Ref. [3].

IV. SUMMARY OF THE DATABASES

In this section we outline data spanning 0.5 to 80 MeV used in the DOM analyses. The $^{209}\text{Bi}(n,n)$ $\sigma(\theta)$ data were obtained from Olsson *et al.* [18,19] at 1.47, 1.96, 2.45, 2.96,

3.47, 4.0, and 21.6 MeV; Lawson *et al.* [8] at 4.5, 5.0, 5.5, 6.0, 6.5, and 7.0 MeV; and Das and Finlay [9] at 7.5, 8.0, 9.0, 10.0, 11.0, 12.0, 20.0, and 24.0 MeV. The compound-elastic contribution was removed from each $^{209}\text{Bi}(n,n)$ $\sigma(\theta)$ datum from 1.47 to 6.5 MeV. The $^{209}\text{Bi}(n,n)$ $A_y(\theta)$ data of the present work are at 6.0 and 9.0 MeV. Energy-averaged total cross sections σ_T for ^{209}Bi were obtained from Finlay *et al.* [20] from 4.5 to 80 MeV and Cierjacks *et al.* [21] from 0.4 to 4.5 MeV. Additional energy-averaged σ_T data from 0.1 to 0.4 MeV were taken from Ref. [22] to be used for comparing predictions of the model.

The $^{208}\text{Pb}(n,n)$ $\sigma(\theta)$ data were obtained from Annand *et al.* [3] at 4.0, 4.5, 5.0, 5.5, 6.0, 6.5, 7.0, and 8.0 MeV; Roberts *et al.* [2] at 9.0 MeV; Floyd *et al.* [23] at 10.0, 14.0, and 16.9 MeV; Finlay *et al.* [24] at 11.0, 20.0, 22.0, and 24.0 MeV; Rapaport *et al.* [25] at 25.7 MeV; and DeVito [26] at 30.3 and 40.0 MeV. Compound-elastic contributions were removed from $^{208}\text{Pb}(n,n)$ $\sigma(\theta)$ data from 4.0 to 7.5 MeV. The $^{208}\text{Pb}(n,n)$ $A_y(\theta)$ data were obtained from Roberts *et al.* [2] at 6.0, 7.0, 8.0, 9.0, and 10.0 MeV and Floyd *et al.* [23] at 10.0 and 14.0 MeV. Average total cross sections σ_T for ^{208}Pb were obtained from Shutt *et al.* [27] from 2.0 to 80 MeV; Fowler *et al.* [28] from 0.7 to 1.89 MeV; Foster *et al.* [29] from 2.49 to 14.9 MeV, and Farrell *et al.* [30] from 0.1 to 1.01 MeV. Here again, the data below 0.5 MeV were only used to compare with model predictions.

V. DOM FORMALISM

The optical-model potential (OMP) may be written as

$$\begin{aligned} U(r,E) = & -[V_V(E) + W_V(E)]f_{\text{WS}}(r,R_V,a_V) \\ & -[V_S(E) + W_S(E)]g_{\text{WS}}(r,R_S,a_S) \\ & -[V_{\text{SO}}(E) + iW_{\text{SO}}(E)] \\ & \times \left(\frac{\hbar}{m_\pi c}\right)^2 \frac{1}{r} g_{\text{WS}}(r,R_{\text{SO}},a_{\text{SO}})(l \cdot \sigma), \end{aligned} \quad (3)$$

where the successive complex-valued terms are the volume-central, surface-central, and spin-orbit potentials. The volume shape is a standard Woods-Saxon form factor specified by a potential radius R_i and diffuseness a_i :

$$f_{\text{WS}}(r,R_i,a_i) = \frac{1}{1 + \exp[(r - R_i)/a_i]}. \quad (4)$$

The surface shape is the first derivative of the Woods-Saxon form:

$$g_{\text{WS}}(r,R_i,a_i) = -4a_i \frac{d}{dr} f_{\text{WS}}(r,R_i,a_i). \quad (5)$$

We introduce the parameter r_i , as defined by the relation $R_i = r_i A^{1/3}$. In our formulation of the OMP in Eq. (3) the real and imaginary volume terms share the same r_V and a_V parameters and likewise the real and imaginary surface terms share the same r_S and a_S . Note also that our r_i and a_i are independent of energy.

The dispersion relation for a complex-valued OMP is given by

$$\Delta V(E) = \frac{P}{\pi} \int_{-\infty}^{+\infty} \frac{W(E')}{E' - E} dE', \quad (6)$$

where W is the imaginary part of the OMP and ΔV is the real-valued “dispersive correction” to the OMP.

The total real-valued part of the dispersive OMP is $V(r, E) = V_{\text{HF}}(r, E) + \Delta V(r, E)$. The dispersive correction ΔV is small relative to the Hartree-Fock nuclear mean field V_{HF} . The present model makes use of volume- and surface-shaped imaginary terms, $W_V(r, E)$ and $W_S(r, E)$, respectively, which gives rise through Eq. (6) to volume and surface dispersive corrections, $\Delta V_V(r, E)$ and $\Delta V_S(r, E)$, respectively. Using the definitions of Eq. (3), the real part of the DOM potential is given by $V(r, E) = V_V(r, E) + V_S(r, E)$, with $V_V(r, E) = V_{\text{HF}}(r, E) + \Delta V_V(r, E)$ and $V_S(r, E) = \Delta V_S(r, E)$.

Note that although the R_V , a_V , R_S , and a_S are independent of energy, because the relative strengths of the two terms $\Delta V_V(r, E)$ and $\Delta V_S(r, E)$ vary greatly with energy, the effective geometry is modulated. This reproduces an important behavior observed in standard OMP's known as the “Fermi surface anomaly,” in which the radius of the real potential must increase as $E \rightarrow 0$ in order to fit $n + {}^{208}\text{Pb}$ scattering data properly. It was shown in Ref. [31] that the dispersion relation accounts for this geometry change by virtue of the $\Delta V_V(r, E)$ and $\Delta V_S(r, E)$ terms, particularly the latter.

Consider a nuclear system $n + A$, where A is the target nucleus. The Fermi energy E_F is defined as lying half-way between the first particle state $E_+ > E_F$ and the first hole state $E_- < E_F$ of the $n + A$ system:

$$E_F = \frac{1}{2} (E_+ + E_-). \quad (7)$$

For the two nuclei under study, the relevant parameters (in MeV) are for $n + {}^{208}\text{Pb}$, $E_+ = -3.94$, $E_- = -7.37$, $E_F = -5.65$; and for $n + {}^{209}\text{Bi}$, $E_+ = -4.50$, $E_- = -7.45$, $E_F = -5.98$. Following Mahaux and Sartor [1], the energy dependence of the Hartree-Fock part of the nuclear mean field is taken as that found by Lipperheide [32]:

$$V_{\text{HF}}(E) = A_{\text{HF}} \exp\left(-\frac{B_{\text{HF}}}{A_{\text{HF}}}(E - E_F)\right), \quad (8)$$

where the parameters A_{HF} and B_{HF} are undetermined constants. The energy dependence of the volume imaginary term W_V is taken to be the form first suggested by Brown and Rho [33] and utilized by Jeukenne and Mahaux [34]:

$$W_V(E) = \frac{A_V(E - E_F)^n}{(E - E_F)^n + (B_V)^n}, \quad (9)$$

where we restrict n to be an even power 2, 4, or 6. The values of n , A_V , and B_V are to be determined by fitting scattering data. We use the W_S energy dependence suggested by Delaroche *et al.* [35] which utilizes the Brown-Rho shape modified by an exponential falloff:

$$W_S(E) = \frac{A_S(E - E_F)^m}{(E - E_F)^m + (B_S)^m} \exp(-C_S|E - E_F|). \quad (10)$$

m is an even power 2, 4, or 6, to be determined along with A_S , B_S , and C_S .

Two important assumptions are made in defining $W_V(E)$ and $W_S(E)$ in most of the previous DOM analyses. First, the $W(E)$ are assumed to be zero at $E = E_F$ and nonzero everywhere else. Second, both $W(E)$ are assumed to be symmetric about the Fermi energy, that is

$$W(E_F - E) = W(E_F + E). \quad (11)$$

In the course of the ${}^{209}\text{Bi}(n, n)$ and ${}^{208}\text{Pb}(n, n)$ DOM analyses reported here, these two assumptions will be modified.

A more realistic parametrization of W_V and W_S forces these terms to be zero in some region around the Fermi energy. A physically reasonable energy for defining such a region is the average energy of the particle states [1]:

$$E_p = \frac{1}{N} \sum_{i=0}^N E_i, \quad (12)$$

where N is the number of single-particle states. (For ${}^{208}\text{Pb}$ the $N = 7$.) We define the “offset energy” E_{offset} for both the particle and the hole region by the relation:

$$E_{\text{offset}} = E_p - E_F. \quad (13)$$

Since $E_F = -5.65$ MeV and $E_p = -2.39$ for ${}^{208}\text{Pb}$, the $E_{\text{offset}} = 3.26$ MeV. Therefore, one writes a new definition for W_V for $E > E_F$:

$$W_V = 0, \quad \text{for } E_F < E < E_p,$$

$$W_V = A_V(E - E_p)^n / [(E - E_p)^n + B_V^n], \quad \text{for } E_p < E, \quad (14)$$

and likewise for W_S . The symmetry condition in Eq. (11) is used to define W_V and W_S for $E < E_F$.

The second assumption that we modify concerns the symmetry of the imaginary potential terms used in the dispersion integrals. Assuming symmetry about the Fermi energy for all energies is equivalent to assuming that W_V and W_S are local potentials [1]. First, we turn to the imaginary volume potential. At large negative energies the volume absorption decreases due to the fact that the nucleon-nucleon (NN) interaction decreases in strength, which may be demonstrated in a meson-exchange perturbation expansion for nuclear matter. The following parametrization was chosen in Refs. [1,36] for ${}^{208}\text{Pb}$ and ${}^{40}\text{Ca}$ for $E < (E_F - 60)$:

$$\mathcal{W}_V(E) = W_V(E) - W_V(E_F - 60) \frac{(E - E_F + 60)^2}{(E - E_F + 60)^2 + 60^2}, \quad (15)$$

where \mathcal{W}_V denotes the nonlocal imaginary volume potential to be used in the dispersion integral. Note that this functional form is chosen in such a way that its first derivative is continuous at $E = (E_F - 60)$. At large positive energies nucleons sense the “hard core” repulsive region of the NN interaction. Using a model of a dilute hard sphere Fermi gas the imaginary potential increases as $\alpha E^{1/2}$, where $\alpha = 1.65$. Adopting this energy dependence, the imaginary volume po-

tential to be used in the dispersion integral is given the following parametrization [1] for $E > (E_F + 60)$:

$$\mathcal{W}_V(E) = W_V(E) + \alpha \left[E^{1/2} + \frac{(E_F + 60)^{3/2}}{2E} - \frac{3}{2} (E_F + 60)^{1/2} \right]. \quad (16)$$

The extra term is again to maintain a continuous first derivative.

A similar form can be proposed for the surface absorption; however, Mahaux and Sartor [36] have shown, in their analysis of $^{40}\text{Ca}(n,n)$ and $^{40}\text{Ca}(p,p)$, that relaxing the symmetry assumption for W_S has a very small effect on the final parametrization. Therefore, we followed Ref. [1] and only considered the effects of nonlocality in the volume absorption.

VI. DISPERSIVE OPTICAL-MODEL (DOM) ANALYSIS

A. DOM software and search methods

A new version of the search code GENOA [37] was written for the DOM analyses. The code now includes the dispersion integrals and can automatically search on all of the parameters in Eqs. (9) and (10) that define W_V and W_S . In each change of the W parameters, the code calculates ΔV_V and ΔV_S . The dispersive integrals are computed with the Simpson numerical method for $n, m = 6$. In the cases where $n, m = 2$ or 4, the integrations are accomplished in closed form using the relations of Vanderkam [38]. For each data set (i.e., for each energy) the code calculates the quantity:

$$\begin{aligned} \chi^2 = & (F_\sigma)^2 \sum_{i=1}^{N_\sigma} \left[\frac{\sigma^{\text{expt}}(\theta_i) - \sigma^{\text{calc}}(\theta_i)}{\Delta \sigma^{\text{expt}}(\theta_i)} \right]^2 \\ & + (F_A)^2 \sum_{i=1}^{N_A} \left[\frac{A_y^{\text{expt}}(\theta_i) - A_y^{\text{calc}}(\theta_i)}{\Delta A_y^{\text{expt}}(\theta_i)} \right]^2 \\ & + (F_T)^2 \left[\frac{\sigma_T^{\text{expt}} - \sigma_T^{\text{calc}}}{\Delta \sigma_T^{\text{expt}}} \right]^2. \end{aligned} \quad (17)$$

We refer to this quantity as ‘‘chi-squared.’’ Here, $\sigma^{\text{calc}}(\theta_i)$ and $\sigma^{\text{expt}}(\theta_i)$ are the differential cross sections from the OM calculations and experiments, respectively, and $\Delta \sigma^{\text{expt}}(\theta_i)$ is the uncertainty, either assigned by us or as reported. The N_σ and N_A are the number of data points for $\sigma(\theta)$ and $A_y(\theta)$, respectively. The weights F_σ , F_A , and F_T are applied separately for each value of σ_T and for each $\sigma(\theta)$ and $A_y(\theta)$ distribution. The code GENOA finetunes the OMP parameters of interest to minimize the total χ^2 of the entire data set for ^{208}Pb or for ^{209}Bi (see Sec. IV).

The code GENOA does not search on bound-state energies. This was done manually in a successive step (described below) with a computer code obtained from Johnson [39]. His code was automated at TUNL to take the DOM parameters as input and predict the binding energies of the single-particle states for the target nucleus plus a neutron particle and the target nucleus plus a neutron hole. The closed forms of Vanderkam were again used for the dispersion integrations. We refer to this code as BSAUTO. Two quantitative measures of the agreement of the bound state calculation

with the experimental bound-state energies were investigated but we found that the agreement had to be judged qualitatively.

To assist in this qualitative judgement, the effects that changes in the DOM parameters have on the binding-energy predictions were investigated carefully. We stepped individual DOM parameters and produced binding-energy predictions at each value of the parameter under scrutiny. Some examples are displayed in Figs. 7 and 8 for the two most sensitive parameters, r_{SO} and V_{SO} . For the other parameters, a few general qualitative remarks will suffice. An increase of A_{HF} , r_{HF} , or a_{HF} increases the magnitude of all binding energies. Increasing the Hartree-Fock slope B_{HF} increases the ‘‘spread’’ of the binding energies about the Fermi energy, since it increases the potential strength for the hole states and decreases it for the particle states. An increase in the magnitude of the ΔV terms (by increasing the W magnitudes) serves to compress the structure of the particle and hole states toward the Fermi energy. This is due to the skew-symmetric shape of the ΔV about the Fermi energy which ‘‘flattens’’ the net real-central nuclear potential $V(E)$ of Eq. (12) by deepening it for $E > E_F$ and making it more shallow for $E < E_F$. This is particularly true of ΔV_S which is more sharply peaked near the Fermi energy than ΔV_V . Finally, an increase of the V_{SO} strength will increase or decrease the net real-potential strength depending on the l value and the angular momentum substate of a single-particle state. The response of the binding energy to changes in V_{SO} for the seven particle states and first six hole states for ^{208}Pb are displayed in Fig. 8. Note that there is a systematic trend as V_{SO} increases: For the case where the projection of the spin is parallel to the orbital angular momentum, the binding energy increases and for the case where the spin and orbital angular momentum are antiparallel, the binding energy decreases. When r_{SO} is varied in the binding-energy calculations, no simple systematic pattern evolves; this is illustrated in Fig. 7.

The search routine in GENOA did not always converge on the optimum solution when the surface in the multidimensional ‘‘chi-squared space’’ was too flat. In light of this, we forced the values of two particularly troublesome parameters, B_{HF} and C_S , using a grid method. For each combination of B_{HF} and C_S , we did a χ^2 search on all other parameters for both systems, $^{209}\text{Bi}(n,n)$ and $^{208}\text{Pb}(n,n)$.

B. The $^{209}\text{Bi}(n,n)$ and $^{208}\text{Pb}(n,n)$ DOM analyses

Several DOM analyses have been reported for $^{208}\text{Pb}(n,n)$: Johnson *et al.* [31], Finlay *et al.* [40], Roberts *et al.* [2], and Mahaux and Sartor [1]. Two DOM analyses have been reported for $^{209}\text{Bi}(n,n)$: Das and Finlay [9] and Lawson *et al.* [8]. The following improvements have been incorporated in the present analysis: (i) for $^{209}\text{Bi}(n,n)$, inclusion of $A_y(\theta)$ data at 6.0 and 9.0 MeV; (ii) use of smooth functional forms for the imaginary potentials, W_V and W_S , in place of the linearly segmented forms used in the $^{208}\text{Pb}(n,n)$ studies of Ref. [2] and Ref. [31]; (iii) consideration of the two complications to the imaginary potentials described at the end of Sec. V, which are considered in the $^{208}\text{Pb}(n,n)$ analysis of Ref. [1]; (iv) use of the increased computing power at TUNL to determine if exhaustive parameter searching can give significant improvements over

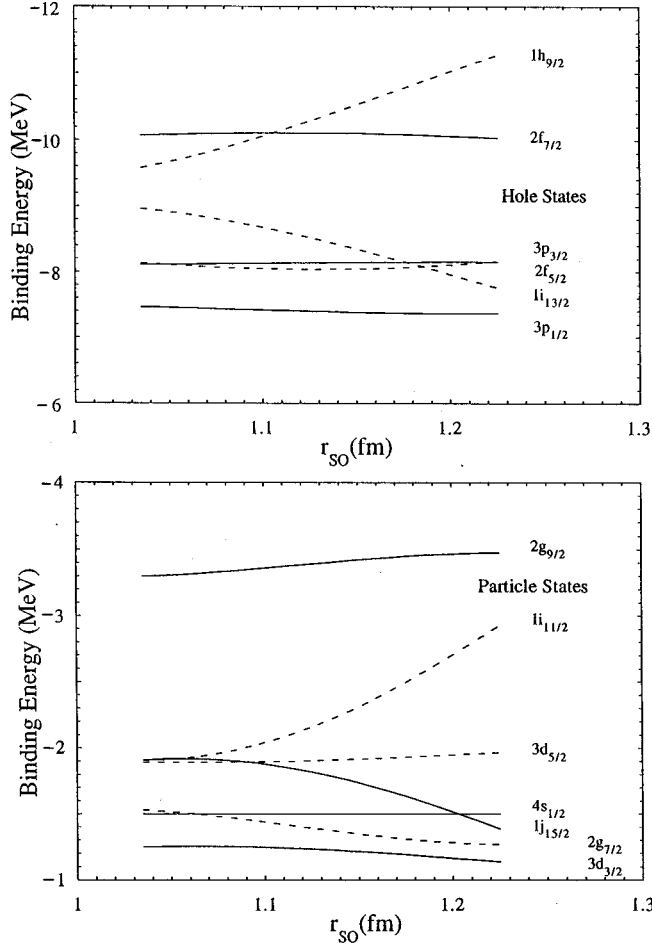


FIG. 7. Binding energies of single-particle states as a function of the r_{SO} parameter.

previous DOM studies; (v) incorporation of proper relativistic corrections for all OM calculations. In regards to the last point, we installed relativistic corrections in GENOA following the method of Schwandt [41]. In all of the previous studies, the relativistic correction is ignored. The effect of the relativistic corrections are 2% to 4% for σ_T between 50 and 80 MeV.

The contents of the DOM databases for ^{209}Bi and ^{208}Pb are given in Sec. IV. The choice of data for ^{208}Pb is virtually identical to that of Roberts *et al.* [2], although we did incorporate the new CN calculations. In the case of ^{209}Bi a couple of additions have been made to the database of Das and Finlay [9]: the present high-accuracy $A_y(\theta)$ data and high-accuracy σ_T data obtained by Finlay *et al.* [20]. In critiquing all the available $n + ^{209}\text{Bi}$ total cross-section data, the following were found to be inconsistent with the rest of the data set and were ignored in our analysis: Das *et al.* [9] for $0.8 < E < 1.0$ MeV and for $45 < E < 60$ MeV and Cierjacks [21] for $20 < E < 31.9$ MeV.

Turning now to the final fitting procedures, we will combine the reports on the DOM for $^{209}\text{Bi}(n,n)$ and $^{208}\text{Pb}(n,n)$. One of the primary objectives of this study was to fit both the $^{209}\text{Bi}(n,n)$ and $^{208}\text{Pb}(n,n)$ databases by using as many common DOM parameters as possible. We did this by compromising between the two models for each parameter successively. Because the general form of the energy

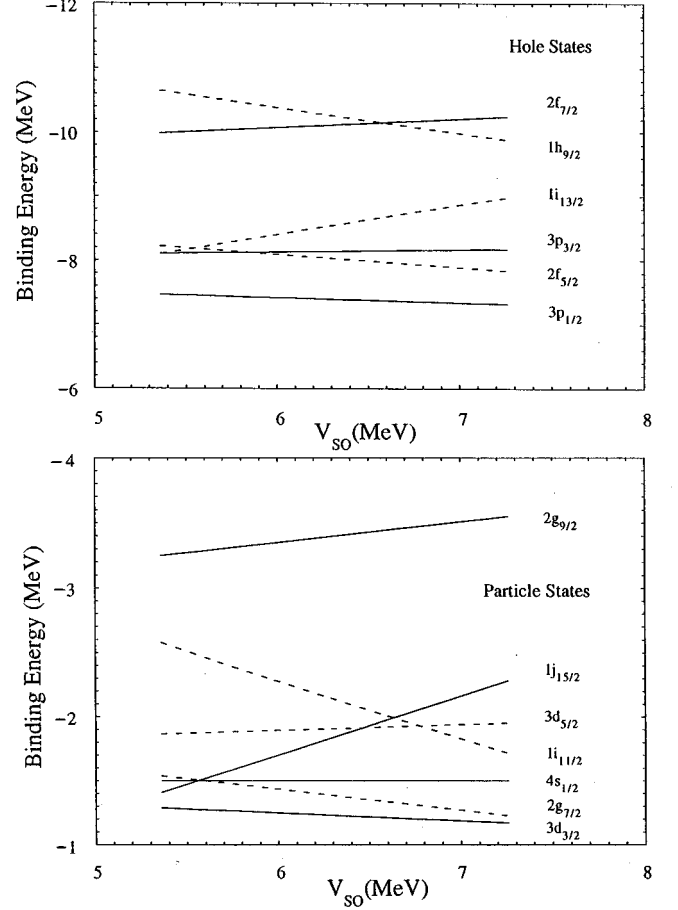


FIG. 8. Binding energies of single-particle states as a function of the V_{SO} parameter.

dependence of the potentials used in the present model is identical to the $^{209}\text{Bi}(n,n)$ DOM of Das and Finlay [9], we used their parameters as a starting point for both nuclei.

In initial search tests, the parametrizations for W_V and W_S were taken as in Eqs. (9) and (10), i.e., with $E_{\text{offset}} = 0$. It was found during a complete search on all DOM parameters that the addition of an offset as in Eqs. (13) and (14) did not affect the quality of the fits to the scattering data. Following Mahaux and Sartor [1] for ^{208}Pb , we used $E_{\text{offset}} = 3.26$ MeV, which is the magnitude of the difference between $E_F = -5.65$ MeV and the average of the ^{208}Pb particle states, $E_p = -2.39$ MeV. Since no useful experimental data for single-particle (or -hole) state information is available for $n + ^{209}\text{Bi}$, we used the offset of $n + ^{208}\text{Pb}$ for the ^{209}Bi calculations. So, from Eq. (13) we obtain for ^{209}Bi the value $E_p = -5.98 + 3.26 = -2.72$ MeV.

Recall that we defined ‘‘ n ’’ to be the power law of W_V and ‘‘ m ’’ to be the power law of W_S in Eqs. (9) and (10), respectively. We first established a common power law for the DOM’s for ^{208}Pb and ^{209}Bi . Various combinations of the powers for n and $m = 2, 4,$ and 6 were attempted. The starting parameters $n/m = 4/4$ were taken from Das and Finlay. Since parametrizations involving the power 6 did not yield any obvious improvements in initial tests, these combinations were eliminated. For each of the remaining n/m combinations, GENOA was allowed to search on all other DOM

parameters to obtain the best chi-squared fit to scattering data. The resultant parameters were then used in BSEAUTO to predict the bound state energies. The n/m combination 2/4 was quickly rejected because it provided relatively poor fits to scattering data. The n/m combination 4/4 gave good fits to scattering or bound-state energies individually but not to both simultaneously. Both the $n/m=2/2$ and 4/2 combinations were capable of yielding excellent fits to scattering data and bound-state energies simultaneously. The 4/2 case was chosen for two reasons: first, the chi-squared results for $n/m=4/2$ were always slightly better. Second, for the $n/m=2/2$ case the C_S parameter often drifted to unphysical values. For ^{208}Pb , C_S became so low in free searches as to produce W_S slopes in the high energy region that were 1/5 that of a typical global model [42–45]. From the $B_{\text{HF}}-C_S$ grid search for $n/m=4/2$, the most promising region of B_{HF} values was 0.340–0.360 for both nuclei, corresponding to C_S values of 0.011–0.014 for ^{208}Pb and 0.019–0.021 for ^{209}Bi .

In the course of the above calculations, the optimum volume and surface geometry parameters could be specified. The values $r_V=1.230$, $a_V=0.688$, $r_S=1.280$, and $a_S=0.503$ were chosen as a good compromise between the two nuclei. These values are within 5% of the values obtained in the individual searches for ^{208}Pb and ^{209}Bi . Upon forcing these geometry parameters into the global search routine, there was a small increase in the total chi-squared of about 5% for both nuclei.

A determination of the spin-orbit parameters was then made. The standard linear energy dependence was used for the spin-orbit parametrization: $V_{\text{SO}}=A_{\text{SO}}+B_{\text{SO}}E$. Throughout the present work, $B_{\text{SO}}=-0.015$ was fixed at the value of the global optical model of Walter and Guss [45]. Their database contained a careful choice of the best neutron data available for $A_y(\theta)$ as of 1985, and their model was constrained to connect with the proton OM of Schwandt *et al.* [46] for $80<E<180$ MeV. In determining the other spin-orbit parameters the ^{209}Bi model had to be guided with the spin-orbit geometry of the ^{208}Pb model since the latter contained more $A_y(\theta)$ data. After a few iterations between the two nuclei, the compromise spin-orbit parameters were determined as $A_{\text{SO}}=6.200$, $B_{\text{SO}}=-0.015$, $r_{\text{SO}}=1.126$, and $a_{\text{SO}}=0.559$. The setting of these parameters brought about insignificant increases (about 1%) in the chi-squared of $A_y(\theta)$ data, in comparison to that for ^{208}Pb and ^{209}Bi separately.

With the above eight parameters determined, the ^{208}Pb DOM was fine tuned to optimize the prediction of the ^{208}Pb bound state energies. The strength A_{HF} for the ^{208}Pb DOM had to be decreased by about 2% for the DOM-predicted first-particle and first-hole states to be centered about the Fermi energy as defined by Eq. (7). The slope of the average mean field B_{HF} then had to be increased from 0.340 to a value of 0.350 to provide a favorable ‘‘spread’’ of all particle and hole states about $E=E_F$. This fixed the two mean-field parameters for ^{208}Pb .

For ^{209}Bi , the same $B_{\text{HF}}=0.350$ was used, but the strength A_{HF} was determined from the ^{208}Pb strength by considering the isospin dependence of the real-central potential. The isovector dependence of the real part of the OMP is param-

eterized in the standard way by the term $V_1(N-Z)/A$. We estimate that $V_1=16.5$ MeV from the Walter-Guss global optical model [44]. From this term, the real part of the potential for ^{209}Bi must be 0.10 MeV higher in magnitude than the potential for ^{208}Pb . However, in applying this difference, note that we must also consider the fact that there is a difference in E_F for the two nuclei in Eq. (8). The nucleus ^{209}Bi has a lower E_F than ^{208}Pb by $\Delta E_F=0.33$ MeV and so its Hartree-Fock strength A_{HF} must be higher than that for ^{208}Pb by $B_{\text{HF}}\times\Delta E_F=0.12$ MeV. Therefore, A_{HF} for ^{209}Bi must be a total of 0.22 MeV larger than that for ^{208}Pb . The final mean-field parameters used in Eq. (8) were $A_{\text{HF}}=46.87$, $B_{\text{HF}}=-0.350$ for ^{208}Pb ; $A_{\text{HF}}=47.09$, $B_{\text{HF}}=-0.350$ for ^{209}Bi . Forcing the above values into the DOM did not deteriorate the chi-squared values for the scattering data for either nucleus by more than 5%, after searching on the remaining five DOM parameters. (The isospin dependence of the imaginary potential is poorly determined compared to that for the real potential; it was ignored in the present work.)

At this point, the five parameters remaining to be constrained were A_V and B_V of Eq. (9) and A_S , B_S , and C_S of Eq. (10). It was found that a good compromise could be attained between ^{209}Bi and ^{208}Pb for A_V and B_V , as they were already within 5% of one another. The final average values were $A_V=5.585$ and $B_V=28.498$. A final search was then done on A_S , B_S , and C_S for ^{208}Pb and ^{209}Bi separately. This completed the determination of all 15 DOM parameters for the two nuclei, the results of which are labeled ‘‘partially constrained’’ in the first column of Table II. The five parameters (E_F , A_{HF} , A_S , B_S , and C_S) which differ between ^{209}Bi and ^{208}Pb are in bold face.

Turning now to the quality of the fits to the scattering data, we first discuss those for $^{209}\text{Bi}(n,n)$. The final $\sigma(\theta)$, $A_y(\theta)$, and σ_T ‘‘partially constrained’’ DOM fits are compared to $^{209}\text{Bi}(n,n)$ data in Figs. 9–14. [Recall from Sec. III that the large error bars of the low energy CN-corrected $\sigma(\theta)$ data are due to the uncertainty of the CN calculation.] Overall, the fits to $\sigma(\theta)$ are of high quality and are comparable to those of Das and Finlay [9]. The difficulty both analyses have in describing the 4.0–8.0 MeV $\sigma(\theta)$ data at back angles will be discussed below. The analysis of Ref. [9] adopted the spin-orbit interaction that Finlay *et al.* [24] obtained from a $^{208}\text{Pb}(n,n)$ study. It is noteworthy that predictions of $A_y(\theta)$ for $^{209}\text{Bi}(n,n)$ at 6.0 and 9.0 MeV which make use of the DOM of Ref. [9] agree with the DOM fits reported in the present paper. In fact, the two sets of $A_y(\theta)$ calculations are nearly identical. However, although Ref. [9] achieves good fits to the $\sigma(\theta)$ and $A_y(\theta)$ data, their fit to the σ_T data is inferior to ours. Compared to our fit to the σ_T data, the prediction of Ref. [9] is about 3% higher at the peak at 4 MeV, 4% higher between 10 and 20 MeV, and about 2% lower between 70 and 80 MeV. The data displayed below 0.5 MeV were not used in the DOM parameter search.

The ‘‘partially constrained’’ DOM fits for $^{208}\text{Pb}(n,n)$ are displayed in Figs. 13–18. The present model produces good fits. Comparing the fits of Roberts *et al.* [2] and Mahaux and Sartor [1] to those of the present work, the differences for the $\sigma(\theta)$ and $A_y(\theta)$ data are very slight. All of the existing

TABLE II. Summary of DOM parameters for $^{208}\text{Pb}(n,n)$ and $^{209}\text{Bi}(n,n)$. Potential strengths and energies are given MeV and geometry parameters in fm. The numbers in boldface indicate a difference between the two scattering systems. All potentials use $n=4$, $m=2$, $E_{\text{offset}}=3.26$ MeV.

Common geometries:		Volume: $r_V=1.230$, $a_V=0.688$ Surface: $r_S=1.280$, $a_S=0.503$ Spin orbit: $r_{SO}=1.126$, $a_{SO}=0.559$			
	Partially constrained	Fully constrained	w/ W_{SO}^a	w/ half asym	w/ asym
$^{209}\text{Bi}(n,n)$ with $E_F = -5.98$					
A_{HF}	47.090	47.090	47.090	47.090	47.090
B_{HF}	-0.350	-0.350	-0.350	-0.350	-0.410
A_V	5.585	5.585	5.585	6.234	4.464
B_V	28.498	28.498	28.498	30.076	25.146
A_S	10.031	9.287	10.072	11.153	8.766
B_S	5.259	4.840	5.217	5.985	4.525
C_S	0.0197	0.0162	0.0197	0.0239	0.0124
A_{SO}	6.200	6.200	6.100	6.200	6.200
B_{SO}	-0.015	-0.015	-0.015	-0.015	-0.015
$^{208}\text{Pb}(n,n)$ with $E_F = -5.65$					
A_{HF}	46.870	46.870	46.870	46.870	46.870
B_{HF}	-0.350	-0.350	-0.350	-0.350	-0.410
A_V	5.585	5.585	5.585	6.234	4.464
B_V	28.498	28.498	28.498	30.076	25.146
A_S	8.479	9.287	8.495	9.211	7.620
B_S	4.162	4.840	4.019	4.839	4.248
C_S	0.0128	0.0162	0.0128	0.0161	0.0067
A_{SO}	6.200	6.200	6.100	6.200	6.200
B_{SO}	-0.015	-0.015	-0.015	-0.015	-0.015

^a $W_{SO}=0.791-0.018 E$, $r_{W_{SO}}=1.364$, $a_{W_{SO}}=0.632$ from Ref. [44].

DOM potentials with energy independent geometries have the deficiency of not being able to reproduce the $\sigma(\theta)$ for $4.0 \leq E \leq 8.0$ MeV for angles from 120° to 150° , the same problem that we observed in the above ^{209}Bi calculations. Standard OM potentials with fixed geometry are also unable to describe this data. Several authors [3,31,47] have shown that the low energy data for ^{208}Pb can be described quite well (with the standard OM and the DOM) if the diffuseness a_s of the surface imaginary potential is allowed to drop to about 0.3–0.4 fm around 4–5 MeV. However, our DOM code does not allow us to introduce an energy dependent diffuseness; the dispersion integral in Eq. (6) assumes that $W(E')$ has the same radial form factor for all energies.

A second approach to improve the agreement at low energies has been reported. In the work of Johnson, Horen, and Mahaux [31], an l -dependent surface absorption was introduced into a DOM in order to improve the agreement between the predictions and the data in the above energy and angular region. Later, Jeukenne, Johnson, and Mahaux [47] repeated the l -dependent work of Ref. [31] and carried out the dispersive integration for an energy dependent r_S and a_S for the surface absorption W_S . They observed that the

dispersive contribution ΔV_S , which was obtained by numerical integration, takes on a very complicated shape for energies from 4 to 7 MeV. (See Figs. 15 and 17 of Ref. [47].) Both Johnson *et al.* [31] and Jeukenne *et al.* [47] believe the l -dependent absorption arises because some partial waves have a node while others have an antinode at the nuclear surface where collective excitations are produced. Although the l -dependent model seems justified, based on their arguments, our global DOM code is not capable of handling this feature. It is likely that an l -dependent absorption would improve the $\sigma(\theta)$ agreement for our model in the 5–7 MeV region and the σ_T agreement below 10 MeV (see Figs. 6 and 7 of Ref. [31]).

The present work produces a superior fit to the σ_T data for $n+^{208}\text{Pb}$ compared to the earlier studies made without l -dependent absorptive potentials. The fit of Roberts *et al.* [2] is lower than ours in the 12–24 MeV range by about 3% and in the 50–80 MeV range by about 4%. When comparing our fit to that of Mahaux and Sartor [1], we find that the σ_T database displayed in Fig. 7.9 of their paper appears to be too high-valued in the peak around $E=4$ MeV. Their calculation is about 6% higher than ours, which itself is a bit

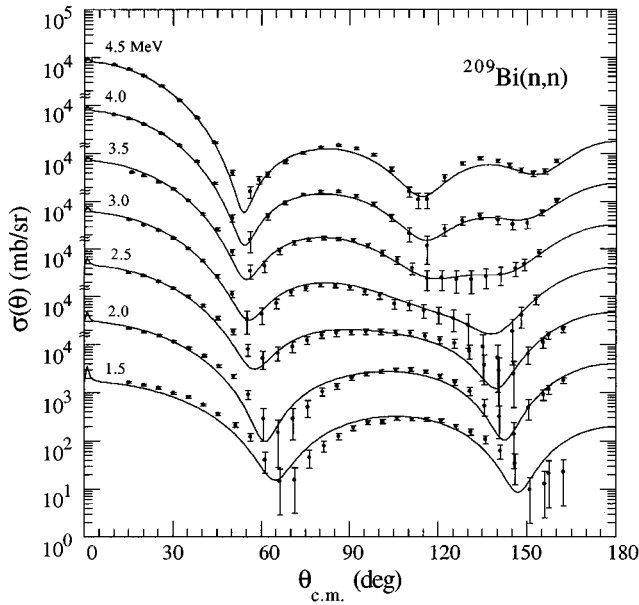


FIG. 9. The $\sigma(\theta)$ $^{209}\text{Bi}(n,n)$ data compared to the “partially constrained” DOM of Table II. The data points represent the shape-elastic contribution, i.e., the measured data minus the calculated CN values.

too high in this region. Their fit also overestimates the data by about 3% in the energy range from 7 to 10 MeV and, as in our case, their fit underpredicts the σ_T around the 18–25 MeV region. Lastly, although their database extends up to $E_n = 40$ MeV, they only display their fit to σ_T up to 25 MeV. In judging the fits of the present DOM relative to those of Refs. [1,2] for ^{208}Pb or those of Das and Finlay [9] for ^{209}Bi , it should be borne in mind that the present study has accomplished improved fits for both nuclei with a parametrization differing in only four parameters between the two nuclei.

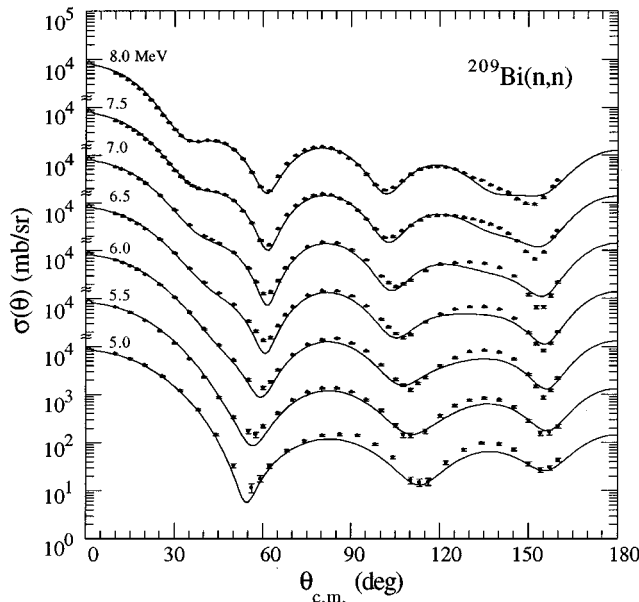


FIG. 10. The $\sigma(\theta)$ $^{209}\text{Bi}(n,n)$ data compared to the “partially constrained” DOM of Table II. The data points below 7.0 MeV have the calculated CN values subtracted.

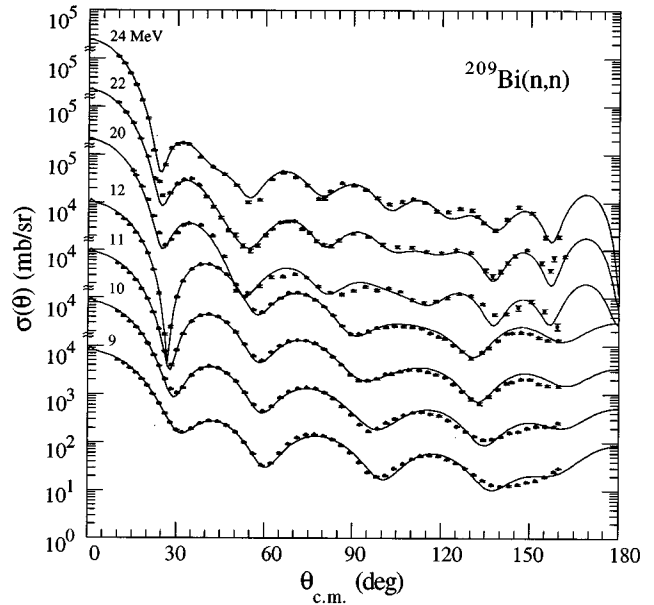


FIG. 11. The $\sigma(\theta)$ $^{209}\text{Bi}(n,n)$ data compared to the “partially constrained” DOM of Table II.

In Table III the final predictions of bound-state energies for neutron-particle and neutron-hole states of ^{208}Pb are listed for the “partially constrained” model. The tabulated bound-state energies from experiment are taken from Johnson *et al.* [31]. Note that the $1h_{11/2}$ state is spread over more than 10 MeV and its binding-energy is not well defined by experiments. (See Fig. 7.26 of Ref. [1] and discussion therein.) The predictions of the present ^{208}Pb DOM lie closer to the experimental values for 11 of the 13 states than do the predictions of Mahaux and Sartor [1], which are included for comparison. Actually, it was surprising that our predicted bound-state energies are so similar to those of Ref. [1] because our “partially constrained” DOM for ^{208}Pb is tightly tied to the equally large amount of scattering data for ^{209}Bi . In addition, we forced our models to fit the high-accuracy σ_T data between 40 and 80 MeV, a region apparently neglected in Ref. [1].

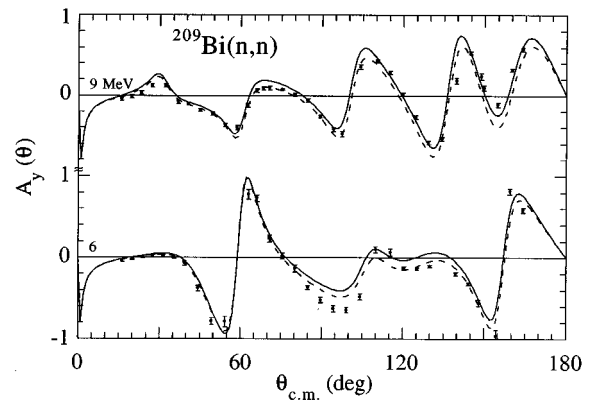


FIG. 12. The $^{209}\text{Bi}(n,n)$ $A_y(\theta)$ data compared to the “partially constrained” (solid curve) and “with W_{SO} ” (dotted) DOM’s of Table II. The data at 6 MeV represent the shape-elastic $A_y(\theta)$ as calculated from Eq. (2).

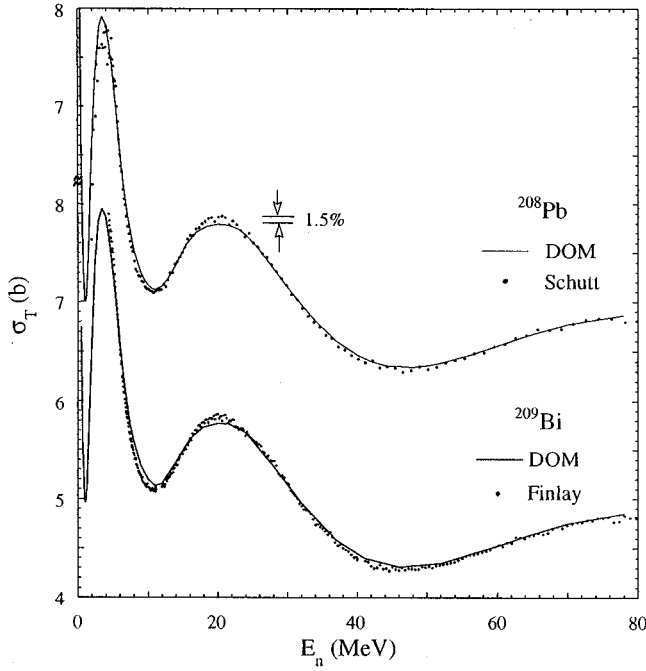


FIG. 13. Bottom plot: The σ_T for $^{209}\text{Bi}(n,n)$ compared to the “partially constrained” DOM of Table II (solid curve). The data are an energy average of Ref. [20]. Top plot: The σ_T for $^{208}\text{Pb}(n,n)$ compared to the “partially constrained” DOM of Table II (solid curve). The data was an energy average of Ref. [27].

In the case of $n + ^{209}\text{Bi}$, the ^{209}Bi “core” is not inert since the scattered neutron now also interacts with a valence proton. The single-particle states lying near the Fermi energy are fragmented and impossible to identify experimentally. Of course, our $n + ^{209}\text{Bi}$ DOM gives bound-state energy predictions which are similar to those for ^{209}Pb ; we do not quote them here.

The small structural differences between our bound-state energy predictions and those of Mahaux and Sartor [1] are probably due to the fact that we use larger V_{SO} and r_{SO} values for the spin-orbit interaction. The model of Mahaux and Sartor takes its spin-orbit parameters from Finlay *et al.* [24], who use $V_{SO} = 5.75$ MeV and $r_{SO} = 1.105$ fm. We found that the choice of larger V_{SO} and r_{SO} values slightly improved certain binding-energy predictions. For example, in our preliminary models, the $1j_{15/2}$ particle state was underbound and appeared above the $3d_{5/2}$ state, which is opposite to the experimentally determined order. Inspection of Figs. 7 and 8 indicates the beneficial effect that an increase of r_{SO} and V_{SO} can have on this problem; our final choice of spin-orbit parameters was influenced by the consideration of both scattering and bound states.

The only question remaining was the source of difference in the W_S parameters appearing in the “partially constrained” column of Table II. These proved to be largely due to the slight differences in the high energy σ_T data for the two nuclei. Much of the ^{209}Bi data in the 50–80 MeV energy range is from Finlay *et al.* [20], while that for ^{208}Pb is from Shutt *et al.* [27]. As is shown on the expanded scale in Fig. 19, the ^{209}Bi data (circles) lie about 1% lower than the ^{208}Pb data (crosses). Within the experimental uncertainties of about 1% on each data set, the σ_T is identical for these

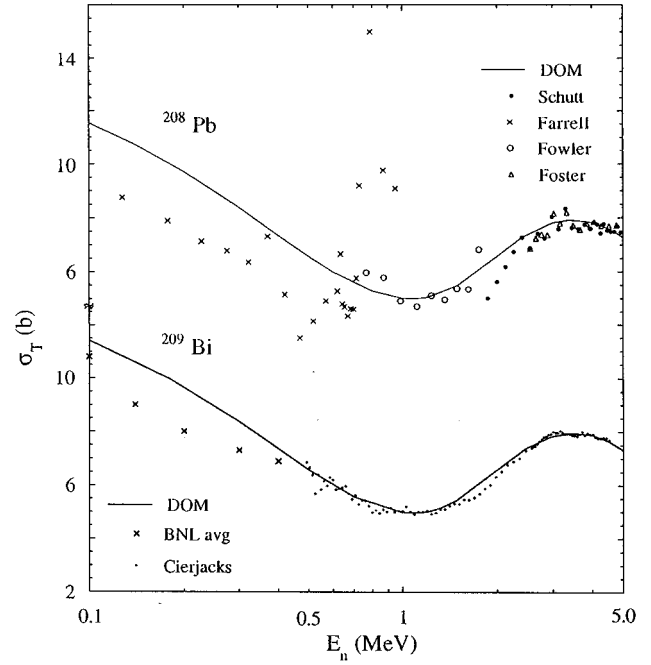


FIG. 14. Bottom plot: The σ_T for $^{209}\text{Bi}(n,n)$ compared to the “partially constrained” DOM of Table II (solid curve). The data are an energy average of Ref. [21] (dots) and Ref. [22]. Top plot: The σ_T for $^{208}\text{Pb}(n,n)$ compared to the “partially constrained” DOM of Table II (solid curve). The data are an energy average of Ref. [27] (dots), Ref. [29] (squares), Ref. [28] (circles), and Ref. [30] (crosses).

isotopes. However, we did not wish to form an average- σ_T database in the 50–80 MeV region.

A “fully constrained” DOM solution was found by repeatedly averaging the respective A_S , B_S , and C_S param-

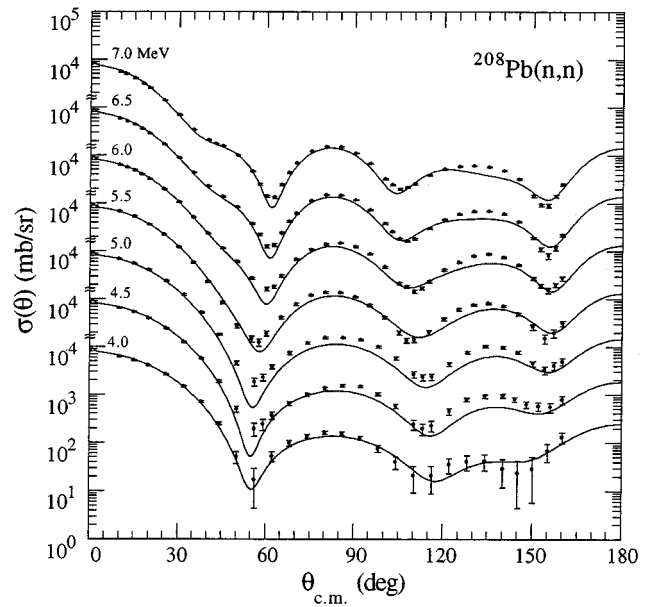


FIG. 15. The $\sigma(\theta)$ data for $^{208}\text{Pb}(n,n)$ compared to the “partially constrained” DOM of Table II. The data points represent the shape-elastic contribution, i.e., the measured data minus the calculated CN values.

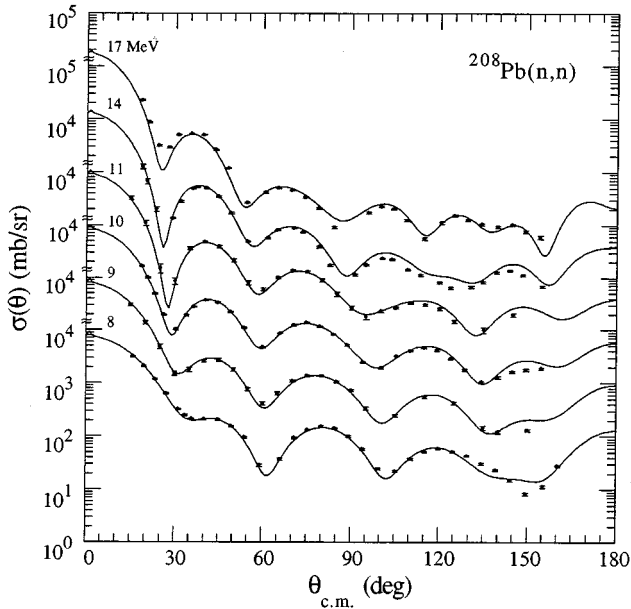


FIG. 16. The $\sigma(\theta)$ data for $^{208}\text{Pb}(n,n)$ compared to the “partially constrained” DOM of Table II.

eters for the ^{209}Bi and ^{208}Pb DOM’s, and retuning. The resulting fits to the 0–40 MeV $\sigma(\theta)$ and $A_y(\theta)$ data are of comparable quality to that obtained in the “partially constrained” DOM. Most of the increase in total chi-squared, of about 12%, was due to the compromise between the two sets of σ_T data. In Fig. 19 we plot the “fully constrained” DOM fits of σ_T , for ^{209}Bi (solid curve) and ^{208}Pb (dotted curve). The DOM parameters are listed in Table II. This model utilizes the same DOM parameters for ^{209}Bi and ^{208}Pb , differing only in the Fermi energy E_F and in the previously calculated small isospin contribution in the Hartree-Fock strength for ^{209}Bi . (The normal $R = r_o A^{1/3}$ dependencies also

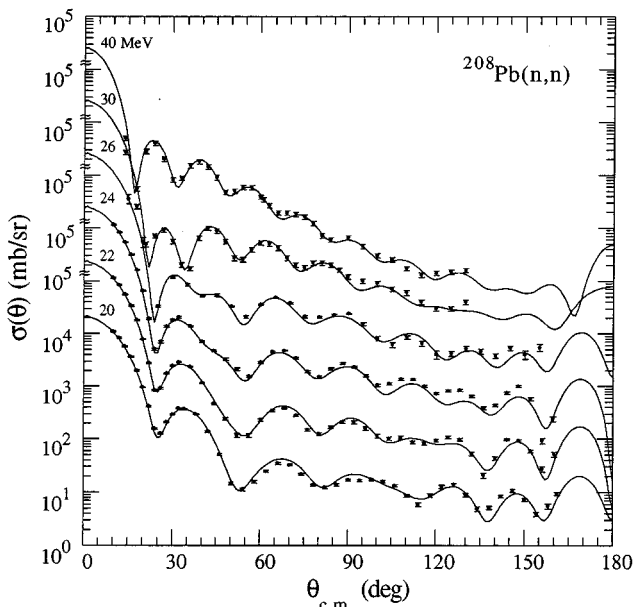


FIG. 17. The $\sigma(\theta)$ data for $^{208}\text{Pb}(n,n)$ compared to the “partially constrained” DOM of Table II.

enter into the difference between the solid and dashed curves in Fig. 19.) We emphasize that this “fully constrained” model fits both sets of $\sigma(\theta)$, $A_y(\theta)$ and σ_T data very well.

The energy dependencies of both constrained DOM potentials are displayed in Figs. 20–22. The $W_V(E)$ and $W_S(E)$ are symmetric about E_F and the $\Delta V_V(E)$ and $\Delta V_S(E)$ are skew-symmetric about E_F ; these functions are graphed in Figs. 21 and 22, but only for $E > E_F$. Figure 20 shows the V_{HF} curves for ^{209}Bi (solid) and ^{208}Pb (dotted), which differ only by the small isospin term and the E_F values. Note that, since E_F enters into Eqs. (9), and (10), the small differences in E_F between ^{209}Bi and ^{208}Pb produce slight differences in W_V , W_S , ΔV_V , and ΔV_S between the $^{209}\text{Bi}(n,n)$ and $^{208}\text{Pb}(n,n)$ models, even when the strength parameters are the same (i.e., the fully constrained model). Figure 21 displays W_V and ΔV_V and Fig. 22 displays W_S and ΔV_S for ^{209}Bi and ^{208}Pb . Note in Fig. 22 that the higher σ_T data for ^{208}Pb forces the imaginary surface potential (dot-dashed curve) to be larger than that for the ^{209}Bi partially constrained model (dashed curve) and thereby causes a less negative ΔV_S term.

C. Further elaborations of the $^{208}\text{Pb}(n,n)$ and $^{209}\text{Bi}(n,n)$ DOM’s

In this section a number of variations will be presented on the “partially constrained” DOM potentials. The first of these, the addition of an imaginary spin-orbit potential W_{SO} , has been of interest in standard optical models for a number of years. The second is specific to the DOM formalization: the relaxation of the symmetry condition of Eq. (11). Table IV lists the percent changes in the total chi-squared resulting in the construction of different versions of the

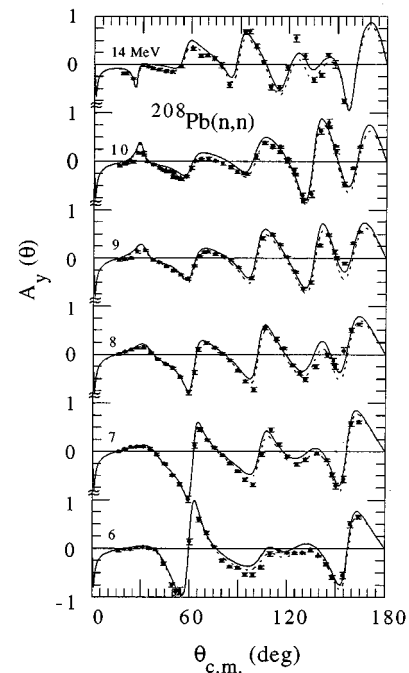


FIG. 18. The $^{208}\text{Pb}(n,n)$ $A_y(\theta)$ data compared to the “partially constrained” (solid curve) and “with W_{SO} ” (dotted) DOM’s of Table II. The data at 6 and 7 MeV represent the shape-elastic $A_y(\theta)$ as calculated from Eq. (2).

TABLE III. Experimental bound-state energies (in MeV) for $^{208}\text{Pb}(n,n)$ and calculations of single-particle properties based on the ‘‘partially constrained’’ DOM potential of Table II.

Bound state	BE expt.	BE present	BE Ref. [1]	S_{nlj} present	N_{nlj} present
$3d_{3/2}$	-1.40	-1.47	-1.44	0.70	0.070
$2g_{7/2}$	-1.44	-1.65	-1.63	0.61	0.096
$4s_{1/2}$	-1.90	-1.70	-1.66	0.73	0.062
$3d_{5/2}$	-2.37	-2.11	-1.98	0.68	0.079
$1j_{15/2}$	-2.51	-2.11	-2.03	0.50	0.128
$1i_{11/2}$	-3.16	-2.43	-2.41	0.56	0.117
$2g_{9/2}$	-3.94	-3.64	-3.54	0.68	0.118
(Model E_F)		($E_F = -5.65$)	($E_F = -5.65$)		
$3p_{1/2}$	-7.37	-7.65	-7.80	0.69	0.82
$2f_{5/2}$	-7.94	-8.29	-8.43	0.65	0.82
$3p_{3/2}$	-8.26	-8.38	-8.48	0.67	0.83
$1i_{13/2}$	-9.00	-8.79	-8.70	0.55	0.80
$2f_{7/2}$	-9.71	-10.34	-10.40	0.63	0.84
$1h_{9/2}$	-10.78	-10.63	-10.57	0.63	0.84
$1h_{11/2}$	-16.5 ± 0.5	-17.42	—	1.13	0.88

$^{209}\text{Bi}(n,n)$ and $^{208}\text{Pb}(n,n)$ DOM’s, relative to the respective ‘‘partially constrained’’ DOM chi-squared.

A number of studies have demonstrated that improved fits to polarization data can be attained with the inclusion of W_{SO} . Previous TUNL work by Roberts *et al.* [2] and Delaroche *et al.* [48] found that a W_{SO} strength of about 0.7 MeV improved the fits to the $A_y(\theta)$ data for $^{208}\text{Pb}(n,n)$. We investigated the inclusion of a W_{SO} as determined in the global model of Walter and Guss [44]:

$$W_{SO} = 0.791 - 0.018E, \quad r_{W_{SO}} = 1.364, \quad a_{W_{SO}} = 0.632. \quad (18)$$

Starting from the ‘‘partially constrained’’ $^{209}\text{Bi}(n,n)$ and $^{208}\text{Pb}(n,n)$ DOM’s, it was found that only three parameters needed to be retuned for each nucleus upon inclusion of the above W_{SO} . The strength of the real spin-orbit potential was dropped from 6.20 to 6.10 MeV for both ^{208}Pb and ^{209}Bi , along with small changes in the W_S parameters A_S and B_S .

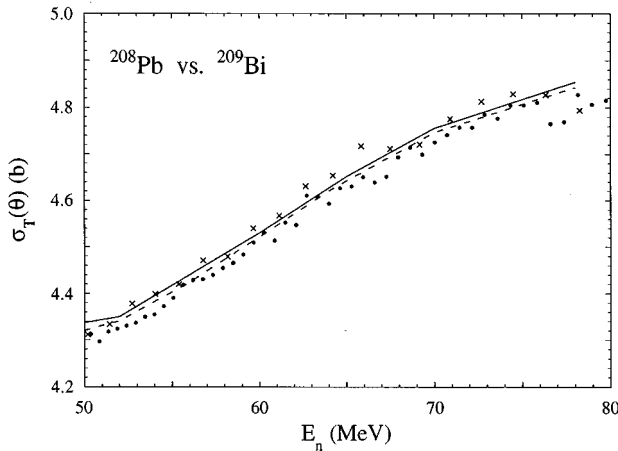


FIG. 19. Total cross-section data compared to the ‘‘fully constrained’’ solution of Table II: ^{209}Bi (circles and solid curve) and ^{208}Pb (crosses and dotted curve). Error bars have been suppressed for clarity. Note the expanded scale.

The new values for these three parameters are listed in the ‘‘w/ W_{SO} ’’ column of Table II. The fits to $\sigma(\theta)$ and σ_T were unaffected by the inclusion of W_{SO} , while the polarization curves showed a marked improvement. As recorded in Table IV, the improvement to the total χ^2 was 6% but the chi-squared for the $A_y(\theta)$ data alone improved by 22% for both DOM models. Figures 12 and 18 for ^{209}Bi and ^{208}Pb , respectively, compare the $A_y(\theta)$ fits of the ‘‘partially constrained’’ DOM’s (solid curves) to those including the W_{SO} of Walter and Guss [44] (dotted curves). The fits including the W_{SO} are clearly superior.

This observation is somewhat in contradiction to that of Delaroche and Tornow [49] for $^{40}\text{Ca}(n,n)$, where it is stated that the ΔV_S dispersive contribution makes W_{SO} unnecessary. However, the present result concurs with the conclusions of Delaroche *et al.* [48] who utilized a standard OM to represent the $^{208}\text{Pb}(n,n)$ data at 10 and 14 MeV, and of Roberts *et al.* [2] who used a DOM formulation. The broader question of the need of an imaginary spin-orbit term for glo-

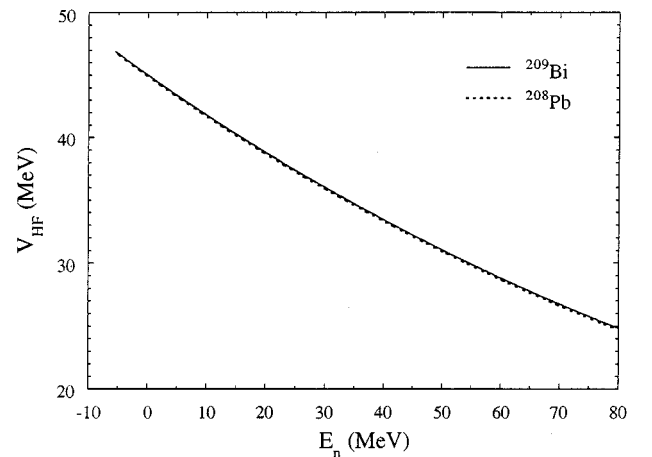


FIG. 20. The V_{HF} for the $^{209}\text{Bi}(n,n)$ (solid) and $^{208}\text{Pb}(n,n)$ (dotted) DOM’s.

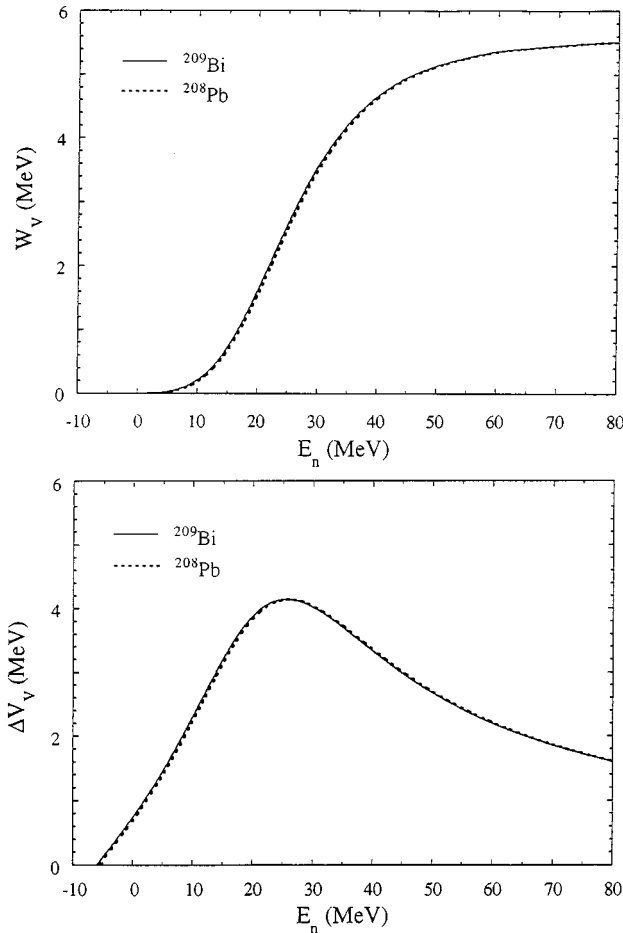


FIG. 21. The W_V and ΔV_V for the $^{209}\text{Bi}(n,n)$ (solid) and $^{208}\text{Pb}(n,n)$ (dotted) DOM's. For these terms there is no distinction between the ‘‘partially constrained’’ and ‘‘fully constrained’’ models solutions of Table II.

bal parametrizations is more controversial than its demonstration for a single nucleus. In the recent global standard OM of Varner *et al.* [45] for neutron energies between 10 and 26 MeV, it is claimed that no W_{SO} is required. Since they biased their neutron model toward higher energy proton scattering data, their conclusion is difficult to interpret. This W_{SO} discrepancy between the two most recent global models for neutron scattering [44,45] leaves the question of the need for a W_{SO} in a global OM for $E < 40$ MeV without a definitive answer. It is also an open question whether the inclusion of the W_{SO} term at low energies compensates for the effect produced by neglecting other physics: e.g., l -dependent absorption [31,47] or channel coupling. These questions notwithstanding, if one utilizes a DOM of the type employed here, the $A_y(\theta)$ data clearly demonstrate the need for a W_{SO} .

The effect of relaxing the symmetry assumption of Eq. (11) for the volume absorption in the dispersion relation was investigated by adopting the parametrizations of Eqs. (15) and (16) for large negative and large positive values, respectively. However, upon the inclusion of the large increase of \mathcal{W}_V above $(E_F + 60)$ MeV, as occurs in Eq. (16) with the Mahaux-Sartor value of $\alpha = 1.65$, the high energy σ_T data of the present DOM database forced some harsh requirements

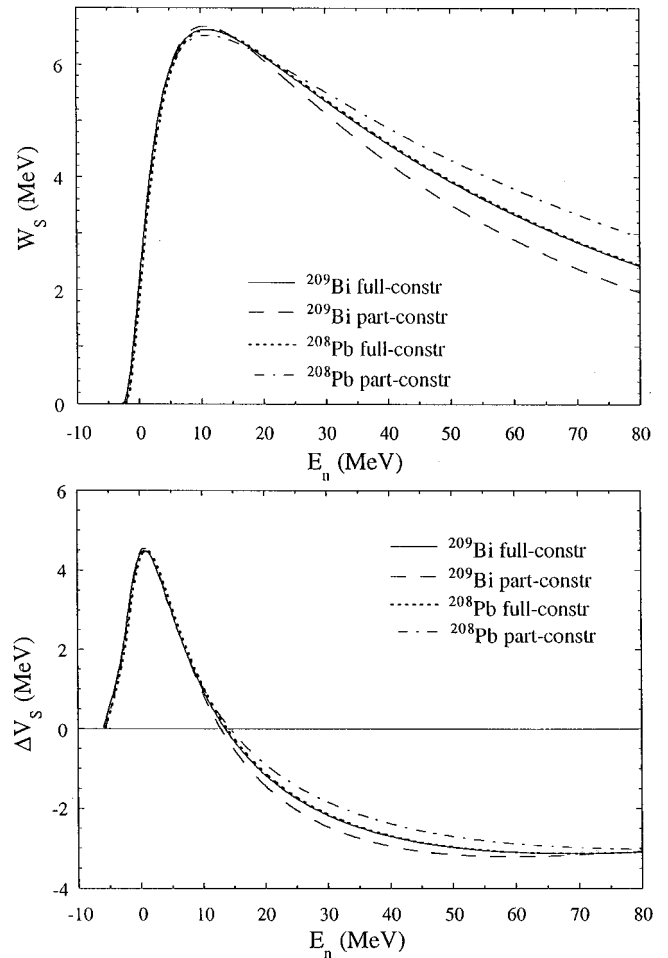


FIG. 22. The W_S and ΔV_S for $^{209}\text{Bi}(n,n)$ (solid curve) and $^{208}\text{Pb}(n,n)$ (dotted) ‘‘fully constrained’’ DOM's, and for $^{209}\text{Bi}(n,n)$ (dashed) and $^{208}\text{Pb}(n,n)$ (dot-dashed) ‘‘partially constrained’’ DOM's.

on the DOM parameters. In the first chi-squared searches with the asymmetric \mathcal{W}_V an extremely high value for the slope of the Hartree-Fock potential was required for both ^{209}Bi and ^{208}Pb : $B_{\text{HF}} \approx -0.450$. Because this spread out the bound-state energy predictions too much about E_F , we changed B_{HF} to -0.410 . Any further reduction of the magnitude of B_{HF} hurt the scattering fits excessively. After the W_V parameters were averaged in the manner described above, a new chi-squared search with $B_{\text{HF}} = -0.410$ yielded significantly lower values for the W_S parameters. These are listed in the ‘‘w/asym’’ column of Table II. The scattering fits only suffered a 15% increase of chi-square, but the bound-state predictions were considerably worsened due to the fact that the $B_{\text{HF}} = -0.410$ requirement distributes the binding energies too widely about the Fermi energy. These results are considered unsatisfactory, especially in view of the peculiar results for the W_S parameters. Note the extremely small result for the C_S of $^{208}\text{Pb}(n,n)$: it would be difficult to give a physical interpretation of why the imaginary surface potential remains at 70% of its maximum value as far out in energy as $E_n = 80$ MeV, as it does here.

To prove that the positive-energy asymmetric term Eq. (16) for the absorption was the source of the problem, the

TABLE IV. Percent change in total chi squared relative to ‘‘partially constrained’’ models of Table II.

	Fully constrained	w/ W_{SO}	w/ half asym	w/ asym
$^{208}\text{Pb}(n,n)$	+13%	-6%	+5%	+19%
$^{209}\text{Bi}(n,n)$	+11%	-6%	-7%	+11%

above procedure was attempted a second time, but with only the negative energy asymmetry term, Eq. (15), included in the dispersion relation. It was found that only the three W_S parameters needed to be retuned to regain good quality fits to both the scattering and bound-state data. These parameters are listed in the fourth column of Table II, labeled ‘‘w/half asym.’’ The fits are virtually identical to those of the ‘‘partially constrained’’ DOM and so are not displayed. It now appears likely that the use of the asymmetric \mathcal{W}_V term by Mahaux and Sartor [1] was ‘‘successful’’ due to the fact that their database stopped at 40 MeV; i.e., they did not have the σ_T constraints imposed on it in the 40–80 MeV range, as does the present DOM. The use of the positive energy \mathcal{W}_V asymmetry, as formulated in Eq. (16), therefore might be restricted to lower energy (<40 MeV) models.

In a paper published since we performed our DOM calculations, Baldo *et al.* [50] investigated more fully the energy dependence of the nonlocal imaginary term. They verified the work in Ref. [1] that \mathcal{W} should go to zero at large negative energies and should be very small by about $E = -300$ MeV. They also demonstrated that the energy dependence of \mathcal{W} for large positive energies is different than Eq. (16) (see Fig. 10 of Ref. [50]). It is not clear how the nuclear matter calculations of Ref. [50] can be incorporated into our DOM formalism. Reference [50] also shows that the contribution to ΔV_V from integrating over energies greater than 500 MeV is significant if one uses a nonlocal \mathcal{W} . However, the effect of the contribution from the integral beyond 500 MeV is small for neutron scattering energies within ± 20 MeV of E_F (see Fig. 14 of Ref. [50]); therefore, the structure calculations for the valence hole and particle states are not affected much by this contribution.

VII. BOUND STATE PROPERTIES

In Table III of Sec. VI B the seven single-particle bound-states and the first seven hole states for neutrons in ^{208}Pb are

TABLE V. Binding energies (in MeV), occupation probabilities, spectroscopic factors, and rms radii (in fm) for two of the particle and two of the hole states.

	$^3d_{3/2}$	$^2g_{9/2}$	$^3p_{1/2}$	$^1h_{9/2}$
Binding energy ^a				
Present work	-1.47 (-1.38)	-3.64 (-3.57)	-7.65 (-7.67)	-10.63 (-10.75)
Mahaux and Sartor [1]	-1.44 (-1.42)	-3.54 (-3.52)	-7.80 (-7.82)	-10.57 (-10.63)
Occupation probability ^a				
Present work	0.070 (0.067)	0.118 (0.112)	0.820 (0.829)	0.836 (0.846)
Mahaux and Sartor [1]	0.08 (0.07)	0.12 (0.11)	0.88 (0.84)	0.89 (0.83)
Spectroscopic factor ^a				
Present work	0.703 (0.702)	0.685 (0.670)	0.689 (0.673)	0.630 (0.622)
Mahaux and Sartor [1]	0.73 (0.72)	0.73 (0.71)	0.73 (0.70)	0.70 (0.67)
rms radii ^a				
Present work	7.63 (7.69)	6.47 (6.47)	6.04 (6.04)	5.97 (5.96)
Mahaux and Sartor [1]	7.76 (7.83)	6.74 (6.80)	6.37 (6.43)	5.84 (5.85)

^aThe first values are for the symmetric and the values in parentheses are for the asymmetric form of \mathcal{W} .

listed along with the experimental values of the bound-state energies and the values calculated with the code BSEAUTO. In 12 out of 14 cases the calculated energies agree to within 400 keV.

The code OCCUP from Ref. [9] was used to calculate spectroscopic factors, occupation probabilities, and root-mean-square radii for the single particles and holes. Table III lists the calculated results for the $n + ^{208}\text{Pb}$ spectroscopic factors S_{nlj} and the occupational probabilities N_{nlj} for the bound-states. In Table V we list the N_{nlj} , S_{nlj} , and the root-mean-square radii for the least-tightly and most-tightly bound particle states, and the least-tightly bound and sixth hole states. The present results are given for the ‘‘partially constrained’’ DOM, for the symmetric W_V and, in parenthesis, for the ‘‘full-asymmetric’’ \mathcal{W}_V . The comparable values obtained by Mahaux and Sartor [1] are also listed. We did not tabulate the single-particle values obtained in Refs. [9,31,51] because, as Mahaux and Sartor [52] point out, a quantity m/m_{HF}^* was omitted from the calculations of Ref. [31,51]. Das and Finlay [9] also omitted this quantity.

VIII. SUMMARY AND CONCLUDING REMARKS

In this paper, we have presented new $^{209}\text{Bi}(n,n) A_y(\theta)$ data at 6.0 and 9.0 MeV. These two distributions are the only high-quality $A_y(\theta)$ data available for the $^{209}\text{Bi}(n,n)$ system. We have also performed a check of calculations of the CN contribution to the (n,n) channel. While our own CN calculations represent a small improvement over past efforts, this study highlighted certain problems that researchers in nucleon-nucleus elastic scattering will have to perennially readdress.

The present DOM analyses, which include the improvements summarized in Sec. VI B, achieved good fits to $\sigma(\theta)$, $A_y(\theta)$, and σ_T data for $^{208}\text{Pb}(n,n)$ and $^{209}\text{Bi}(n,n)$.

The largest difference in the DOM parameters between the two scattering systems exists in the W_S and resulting ΔV_S terms. For our “partially constrained” DOM potentials, $^{208}\text{Pb}(n,n)$ has a higher W_S and ΔV_S than $^{209}\text{Bi}(n,n)$ for $E > 20$ MeV: this was necessary to accommodate the small differences in the σ_T databases. The $^{208}\text{Pb}(n,n)$ “partially constrained” model gives excellent agreement with experimentally determined bound-state energies. Our calculations of the associated spectroscopic factors and occupational probabilities yield results that are similar to those of Mahaux and Sartor [1]. The calculation-intensive searches on DOM parameters in the present work indicate that previous DOM studies of $^{209}\text{Bi}(n,n)$ or $^{208}\text{Pb}(n,n)$ have achieved near optimum fits to $\sigma(\theta)$ and $A_y(\theta)$ data. However, the present “partially constrained” study achieves equivalent fits for differential data of both nuclei while doing significantly better for σ_T data.

The present DOM potentials have also demonstrated the need for an imaginary spin-orbit term. There might be an interest to pursue the possibility of incorporating a W_{SO} within the DOM formalism. However, the small magnitude of a ΔV_{SO} dispersion term (because W_{SO} is small) would make it difficult to unambiguously prove its existence through measurements.

The asymmetric version of the present DOM potentials failed to describe the σ_T data for $E > 40$ MeV. It is possible

that a DOM parametrization can be found which compensates for the sharp increase in potential strength due to the asymmetric W_V term at high energy. The present formula for W_S in Eq. (10) contrasts with the one used by Mahaux and Sartor [1] in their analysis for $E < 40$ MeV. We did not attempt to use their form. We doubt that any high energy dependence of W_S could counter the large Hartree-Fock slope B_{HF} required by the asymmetric W_V term. Furthermore, it is significant that the $^{208}\text{Pb}(n,n)$ analysis in Ref. [1] used no σ_T data above 40 MeV; in the present study, inclusion of this data required drastic changes to the nuclear mean field with the adoption of a nonlocal absorption.

ACKNOWLEDGMENTS

We acknowledge a number of contributions to the present work: D. J. Horen for discussions concerning the comparison of ^{209}Bi and ^{208}Pb and the CN calculations, and also for participating in some of the measurements; J. M. Hanly for supplying a version of the CN code HELGA; J. Vanderkam for accomplishing the dispersion integrations in closed form; and R. W. Finlay for releasing the σ_T data prior to full publication. This work was supported by the U.S. Department of Energy, Office of High Energy and Nuclear Physics, under Grant No. DEFG05-ER40619 with Duke University.

-
- [1] C. Mahaux and R. Sartor, *Adv. Nucl. Phys.* **20**, 1 (1991).
 [2] M.R. Roberts, P.D. Felsher, G.J. Weisel, Zemin Chen, C.R. Howell, W. Tornow, and R.L. Walter, *Phys. Rev. C* **44**, 2006 (1991).
 [3] J.R.M. Annand, R.W. Finlay, and F.S. Dietrich, *Nucl. Phys.* **A443**, 249 (1985).
 [4] G.J. Weisel, Ph.D. Dissertation, Duke University, 1992.
 [5] G.G. Ohlsen and P.W. Keaton, *Nucl. Instrum. Methods* **109**, 41 (1973); G.G. Ohlsen, J.L. McKibben, G.P. Lawrence, P.W. Keaton, Jr., and D.D. Armstrong, *Phys. Rev. Lett.* **27**, 599 (1971).
 [6] P.W. Lisowski, R.L. Walter, C.E. Busch, and T.B. Clegg, *Nucl. Phys.* **A242**, 298 (1975).
 [7] E. Woye, computer code JANE, described in the Ph.D. dissertation, University of Tübingen, 1983.
 [8] R.D. Lawson, P.T. Guenther, and A.B. Smith, *Phys. Rev. C* **36**, 1298 (1987).
 [9] R.K. Das and R.W. Finlay, *Phys. Rev. C* **42**, 1013 (1990).
 [10] M.J. Martin, *Nucl. Data Sheets* **47**, 797 (1986).
 [11] M.J. Martin, *Nucl. Data Sheets* **22**, 545 (1977).
 [12] P.A. Moldauer, *Phys. Rev.* **135**, B642 (1964); **136**, B947 (1964).
 [13] P.A. Moldauer, *Nucl. Phys.* **A344**, 185 (1980).
 [14] A. Gilbert and A.G.W. Cameron, *Can. J. Phys.* **43**, 1446 (1965).
 [15] J.M. Hanly, the University of Kentucky version of the computer code HELGA, private communication, 1987.
 [16] R.K. Das, J.R.M. Annand, and R.W. Finlay, Ohio University computer code OPSTAT, private communication, 1989.
 [17] A.B. Smith, P. Guenther, and J. Whalen, *Nucl. Sci. Eng.* **75**, 69 (1980).
 [18] N. Olsson, B. Holmquist, and E. Ramström, *Nucl. Phys.* **A385**, 285 (1982).
 [19] N. Olsson, B. Trostell, E. Ramström, B. Holmquist, and F.S. Dietrich, *Nucl. Phys.* **A472**, 237 (1987).
 [20] R.W. Finlay, F. Fink, W. Abfalterer, P. Lisowski, G.L. Morgan, and R.C. Haight, in *Nuclear Data for Science and Technology*, Proceedings of the 1991 Jülich Conference, edited by S.M. Qaim (Springer-Verlag, Berlin, Heidelberg, New York, 1992), p. 720. See also *Phys. Rev.* **C47**, 237 (1993).
 [21] S. Cierjacks, P. Forti, D. Kopsch, L. Kropp, J. Nebe, and H. Unseld, Kernforschungszentrum Karlsruhe Report Nos. KFK-1000, EUR-3963E, and EANDC(E)-111, 1968.
 [22] Data obtained from V. McLane, C.L. Dunford, and P.F. Rose, *Neutron Cross Section Curves* (Academic Press, New York, 1988).
 [23] C.E. Floyd, Jr., Ph.D. dissertation, Duke University, 1981; C.E. Floyd, P.P. Guss, R.C. Byrd, K. Murphy, R.L. Walter, and J.P. Delaroche, *Phys. Rev. C* **28**, 1498 (1983).
 [24] R.W. Finlay, J.R.M. Annand, T.S. Cheema, J. Rapaport, and F.S. Dietrich, *Phys. Rev. C* **30**, 796 (1984).
 [25] J. Rapaport, R.S. Cheema, D.E. Barnum, R.W. Finlay, and J.D. Carlson, *Nucl. Phys.* **A296**, 95 (1978).
 [26] R. DeVito, Ph.D. dissertation, Michigan State University, 1979.
 [27] R.L. Schutt, R.E. Shamu, P.W. Lisowski, M.S. Moore, and G.L. Morgan, *Phys. Lett.* **203**, 22 (1988); R.E. Shamu, private communication.
 [28] J.F. Fowler and E.C. Campbell, *Phys. Rev.* **127**, 2192 (1962).
 [29] D.G. Foster, Jr. and D.W. Glasgow, *Phys. Rev. C* **3**, 576 (1971).

- [30] J.A. Farrell, G.C. Kyker, Jr., E.G. Bilpuch, and H.W. Newson, *Phys. Lett.* **17**, 286 (1965).
- [31] C.H. Johnson, D.J. Horen, and C. Mahaux, *Phys. Rev. C* **36**, 2252 (1987).
- [32] R. Lipperheide, *Z. Phys.* **202**, 58 (1967).
- [33] G.E. Brown and M. Rho, *Nucl. Phys.* **A372**, 397 (1981).
- [34] J.P. Jeukenne and C. Mahaux, *Nucl. Phys.* **A394**, 445 (1983).
- [35] J.P. Delaroche, Y. Wang, and J. Rapaport, *Phys. Rev. C* **39**, 391 (1989).
- [36] C. Mahaux and R. Sartor, *Nucl. Phys.* **A528**, 253 (1991).
- [37] Code GENOA obtained from F. Perey of ORNL.
- [38] J.M. Vanderkam, *Bull. Am. Phys. Soc.* **36**, 2730 (1991); J.M. Vanderkam and W. Tornow, TUNL XXX progress report, 1991, p. 101.
- [39] C.H. Johnson, private communication.
- [40] R.W. Finlay, J. Wierzbicki, R.K. Das, and F.S. Dietrich, *Phys. Rev. C* **39**, 804 (1989).
- [41] The corrections are those introduced into SNOOPY by P. Schwandt. For a description see P. Schwandt in IUCF Report No. 85-X, 1985; A. Nadasen *et al.*, *Phys. Rev. C* **23**, 1023 (1981).
- [42] F.D. Becchetti and G.W. Greenlees, *Phys. Rev.* **182**, 1190 (1969).
- [43] J. Rapaport, *Phys. Rep.* **87**, 25 (1982).
- [44] R.L. Walter and P.P. Guss, in *Nuclear Data for Basic and Applied Science*, edited by P.G. Young, R.E. Brown, G.F. Auchampaugh, P.W. Lisowski, and L. Stewart (Gordon and Breach, New York, 1986), Vol. 2, p. 1079.
- [45] R.L. Varner, W.J. Thompson, T.L. McAbee, E.J. Ludwig, and T.B. Clegg, *Phys. Rep.* **201**, 57 (1991).
- [46] P. Schwandt, H.O. Meyer, W.W. Jacobs, A.D. Bacher, S.E. Vigdor, M.D. Kaitchuck, and T.R. Donoghue, *Phys. Rev. C* **26**, 55 (1982).
- [47] J.P. Jeukenne, C.H. Johnson, and C. Mahaux, *Phys. Rev. C* **38**, 2573 (1988).
- [48] J.P. Delaroche, C.E. Floyd, P.P. Guss, R.C. Byrd, K. Murphy, G. Tungate, and R.L. Walter, *Phys. Rev. C* **28**, 1410 (1983).
- [49] J.P. Delaroche and W. Tornow, *Phys. Lett. B* **203**, 4 (1988).
- [50] M. Baldo, I. Bombaci, G. Giansiracusa, U. Lombardo, C. Mahaux, and R. Sartor, *Nucl. Phys.* **A545**, 741 (1992).
- [51] C.H. Johnson and C. Mahaux, *Phys. Rev. C* **38**, 2589 (1988).
- [52] C. Mahaux and R. Sartor, *Nucl. Phys.* **A493**, 157 (1989).